Chapter 2
Novel Excitonic Properties of Carbon Nanotube Studied by Advanced Optical Spectroscopy

Kazunari Matsuda

Abstract Novel excitonic properties of single-walled carbon nanotubes are studied by single-nanotube spectroscopy and time-resolved spectroscopy. Due to the enhanced Coulomb interaction, the optically generated electron-hole pair forms a strongly "bound exciton" state, analogous to the hydrogen-like state in the carbon nanotubes. The exciton properties and dynamics dominate their optical properties. The striking features of excitons in the carbon nanotube, multiple-exciton states, charged exciton (trion) formation, and exciton-multiplication are described in this chapter.

2.1 Basic Optical Properties of Carbon Nanotube

2.1.1 Structure of Carbon Nanotube

The nano-carbon materials consisting from carbon honeycomb lattice have been attracted great deal of interests from viewpoints of basic science and applications. The nano-carbon materials include varieties of materials such as fullerene (C_{60}), carbon nanotube, and graphene. In this chapter, we mainly focus on a single-walled carbon nanotube (SWNT), about 1 nm in diameter and greater than several hundred nanometers in length, is a prototypical system of one-dimensional (1D) structures [1]. SWNTs consist of a two-dimensional (2D), single-layer carbon honeycomb lattice (or graphene sheet) that has been rolled into a cylindrical structure, as shown in Fig. 2.1(a). The SWNT is characterized by the (n, m) index or chiral index (chirality), where n and m are integers [2–5]. The chiral index makes a regulation of the angle and radius, which describe the way in which the graphene sheet is rolled. Figure 2.1(b) shows the schematic of a graphene sheet. The chiral vector C in the graphene sheet can be described as

$$C = na_1 + ma_2, \tag{2.1}$$

K. Matsuda (✉)

Institute of Advanced Energy, Kyoto University, Gokasho, Uji, Kyoto 611-0011, Japan
e-mail: matsuda@iae.kyoto-u.ac.jp
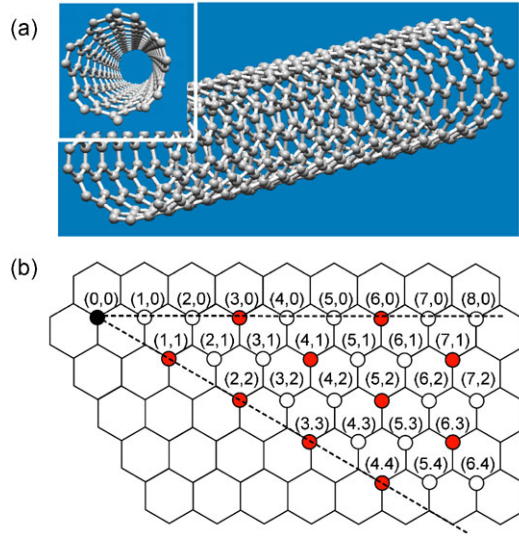
where a_1 and a_2 are fundamental lattice vectors. The structure of SWNTs with chiral index (n, m) can be formed by connecting the origin to point (n, m). The diameter d of SWNTs with chiral index (n, m) can be expressed as

$$d = a\frac{\sqrt{n^2 + m^2 + mn}}{\pi},\tag{2.2}$$

where $a(= |a_1| = |a_2|)$ is 2.46 Å. The most striking feature of SWNTs is that the electronic properties are determined only by the structure of the carbon nanotube itself, i.e., the chiral index (n, m), as described in the next section.

2.1.2 Electronic Structure of Graphene

At first, the electronic structure of graphene should be explained, since the electronic structure of SWNTs can be obtained by zone-folding of that of a graphene. Figure 2.2 shows the reciprocal lattice of graphene in the momentum space and its 1st Brillouin zone. The shape of 1st Brillouin zone at reciprocal space shows the hexagonal shape reflecting the hexagonal periodical lattice of graphene in the real space. The simple tight-binding approximation is useful to understand the electronic structure of the graphene as a first step, where the Coulomb interactions between the electron-electron do not be considered. The unit cell of graphene is defined by the fundamental lattice vectors of a_1 and a_2. The unit cell contains two carbon atoms, and each carbon atom has four electrons in the valence band. The three of these electrons will hybridize forming σ-bonds in the hexagonal plane and one forms a π bond. The π electrons which are delocalized in the crystal, mainly dominate the

Fig. 2.2 Schematic of
reciprocal lattice of graphene
and 1st Brillouin zone
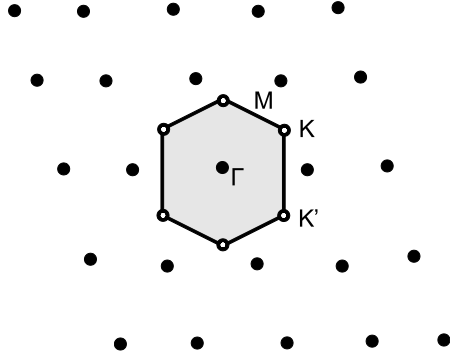
electronic properties. Moreover, taking account only the nearest-neighbor interaction, the energy dispersion relation of the graphene is given by

$$E_g^{\pm} = \pm\gamma_0\sqrt{1 + 4\cos\frac{\sqrt{3}k_x a_0}{2}\cos\frac{k_y a_0}{2} + 4\cos^2\frac{k_y a_0}{2}}, \qquad (2.3)$$

where γ_0 is the nearest-neighbor transfer integral and $\pm$ sign corresponds to the bonding (valence) and anti-bonding (condition) bands in the k space. The energy dispersion of the bonding (valence) and anti-bonding (conduction) bands are symmetric with respect to the Fermi level. Moreover, the energy bands at the K points are degenerated at the Fermi level ($E_g = 0$), which indicates that the graphene is a zero-gap material.

2.1.3 Electronic Structure of Carbon Nanotube

Based on the electronic structure of graphene described in previous section, the zone-folding or confinement approximation of the electronic structure of graphene provides the information on the electronic band structure of SWNTs. The allowed wavevector component around the circumference of SWNTs is quantized, while the component along the nanotube axis is continuous. The zone-folding approximation consists in sectioning the graphene electronic structure as a "cutting line", as shown in Figs. 2.3(a) and (b). Thus, the energy bands for the SWNT will be a series of 1D dispersion relations. The zone-folding approximation provides a simple scheme of the electronic properties, however it still is needed to understand that the some SWNTs have metallic electronic states and the others have semiconducting ones. This characteristic property comes from the energy band dispersion of graphene, with zero-gap at K point. If the K point is an allowed wavevector of SWNTs, i.e. the cutting line is crossed at K point as shown in Fig. 2.3(a), then the SWNTs will be metallic, as shown in the band structure of the lower panel of Fig. 2.3(a). In this case, the structure of SWNTs has a chiral index relationship of $n - m = 3m$ (m: integer). On the other hand, if the K point is not an allowed wavevector of

Fig. 2.3 Schematic of 1st
Brillouin zone with the
cutting lines and energy band
structure in (**a**) metallic and
(**b**) semiconducting carbon
nanotube

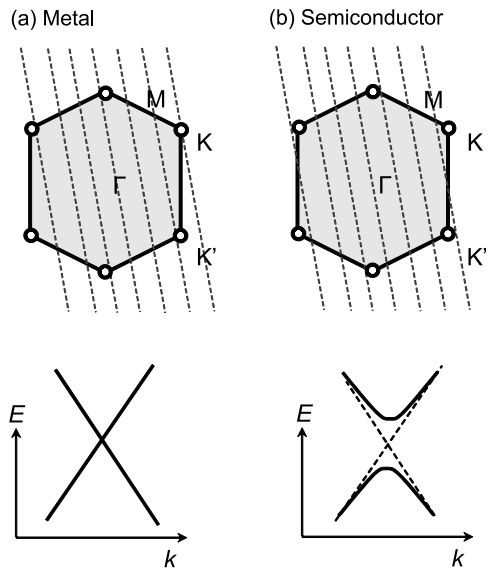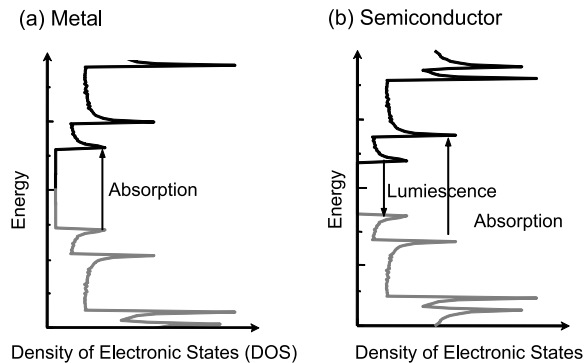(a) Metal   (b) Semiconductor

Fig. 2.4 Density of states of
(**a**) metallic and
(**b**) semiconducting carbon
nanotube. Optical transitions
of absorption and
luminescence are indicated in
the figure

(a) Metal   (b) Semiconductor

SWNTs, i.e. the cutting line is not crossed at K point, then the SWNTs with a chiral index relationship of $n - m \neq 3m$ will be semiconducting. The chiral indices of semiconducting and metallic SWNTs are shown in Fig. 2.1(b). From this simple relationship, the 1/3 of SWNTs have metallic electronic states, while the rest have semiconducting ones.

The density of states is an useful quantity to understand the electronic structures of SWNTs. Figure 2.4 shows the schematic of the density of states (DOS) of metallic ($n - m = 3m$) and semiconducting ($n - m \neq 3m$) SWNTs. The sharp von-Hove singularity peak in the density of states arises from the 1D quantum confined electronic state in the SWNTs. The band-gap energy E_g of semiconducting SWNTs is inversely proportional to the diameter; this is predicted by the simple tight-binding calculation [6].

**Fig. 2.5** Two-dimensional photoluminescence (PL) excitation map of SWNTs
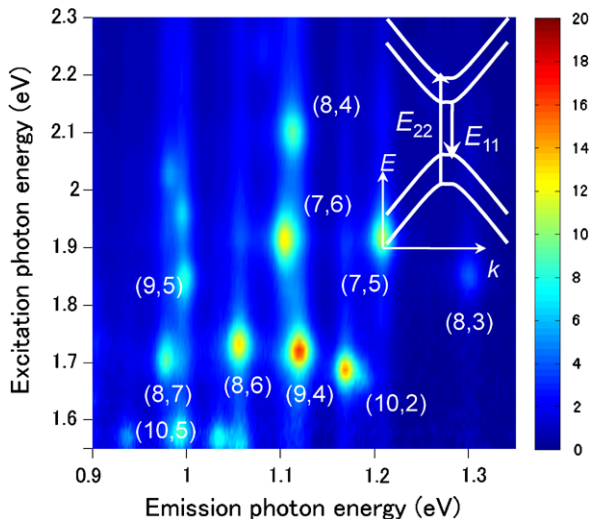
2.1.4 Optical Spectroscopy of Carbon Nanotubes

The optical properties of semiconducting SWNTs have been extensively studied since 2002 when O'Connell reported that micelle-encapsulated semiconducting SWNTs showed very clear photoluminescence (PL) [7, 8]. The observation of PL is due to the isolation of individual SWNTs that are prevented from bundling with semiconducting and metallic carbon nanotubes [7, 9]. This is because that the energy transfer between the semiconducting and metallic carbon nanotubes is occurred and optically excited carriers are non-radiatively quenched at the metallic carbon nanotubes in the bundled samples [7, 9]. Indeed, it has been reported that the isolated air-suspended carbon nanotubes fabricated between the Si pillars also showed clear PL signals [9].

Figure 2.5 shows the typical 2D PL excitation (PLE) map corresponding to the contour plot between the excitation energy (wavelength) and PL spectra of micelle-encapsulated SWNTs [8]. Several PL signals, shown as spots, are observed in the 2D PL map, which indicates the sharp resonance features of the SWNT electronic states. The photon energy of the PLE signals on the vertical axis corresponds to the optical absorption peak between the second sub-band of the conduction to valence state, as indicated by E_{22} in the inset of Fig. 2.5. In contrast, the energy of the peak on the horizontal axis corresponds to E_{11}, the PL energy corresponding to the band gap of semiconducting SWNTs. The energies E_{11} and E_{22} in (n, m) SWNTs can be calculated using the tight-binding method. From the predicted E_{11} and E_{22} energies, one can assign each peak in the 2D PLE map to (n, m) of the SWNTs, as indicated in Fig. 2.5 [10]. Most researchers in this field have believed that the PL signal from semiconducting SWNTs comes from the recombination of the optically-excited free electron in the conduction band and free hole in the valence band. In this one-electron picture, shown in Fig. 2.6(a), without consideration

Fig. 2.6 Schematic of
electronic structures of
SWNTs in (**a**) the
one-electron picture without
Coulomb interactions and
(**b**) the exciton picture with
Coulomb interactions

(a) One-electron

(b) Exciton

n=∞
n=3
n=2

Binding
energy

n=1

E

Exciton

K

k
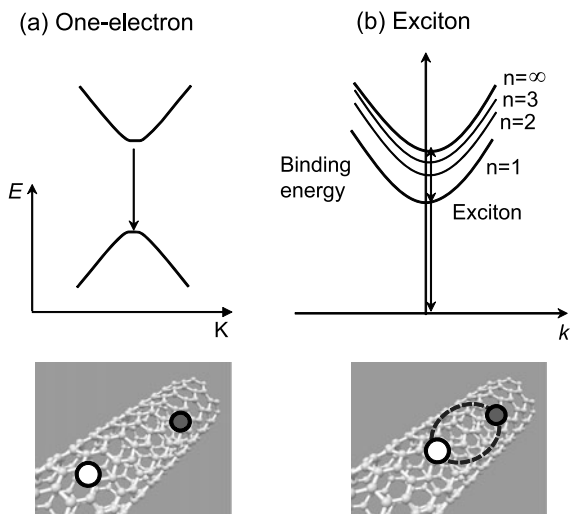
of Coulomb interactions, the resonance features of the optical spectra are attributed
to the sharp electronic states corresponding to the 1D von-Hove singularity. In con-
trast, Ando theoretically pointed out that the Coulomb interaction between the elec-
tron and hole pair is greatly enhanced in the 1-nm cylindrical structure and, in fact,
that the Coulomb interaction affects the optical spectrum of SWNTs [11], as de-
scribed in the next section.

2.1.5 Exciton State in Carbon Nanotubes

The attractive Coulomb interaction between the optically excited electron and hole
pair plays an important role in understanding the optically excited states in the solid.
When the electron and hole are strongly confined in the 1D system such as the
SWNTs with only 1 nm diameter, the attractive Coulomb interaction between the
electron and hole is much enhanced in comparison with 3D bulk materials. The en-
hanced Coulomb interactions in 1D SWNTs lead to the formation of tightly bound
electron-hole pairs, i.e., "excitons", analogous to a hydrogen-like state in the solid,
as shown in Fig. 2.6(b) [11–17]. The exciton has the series of energy structure, as
similar to the hydrogen atom, $n = 1, 2, 3, \ldots$, where n is the quantum number. The
energy position of $n = \infty$ corresponds to the free electron and hole pair energy,
i.e. band gap energy E_g. The stable energy due to formation of the exciton corre-
sponds to the energy difference between $n = 1$, and $n = \infty$, which is defined as the
exciton binding energy. The exciton binding energy in the typical bulk compound
semiconductor ranges from a few to several-tenth meV.

Following theoretical studies [9–15], the optical experiments were carried out to
reveal the excitons in the SWNTs. The simple tight-binding calculation without con-
sidering the Coulomb interaction predicts that the energy ratio of E_{22}/E_{11} should

(a) |K;K> (b)|K;K'> (c) |K';K'> (d)|K';K>
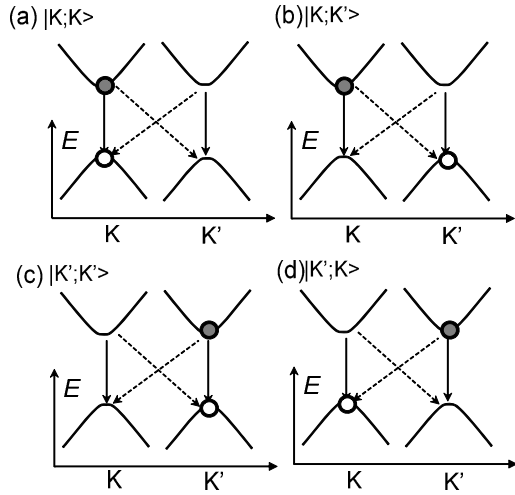
be factor of 2, however it has been well known that the experimentally obtained E_{22}/E_{11} were deviated from the factor 2. This is called as "ratio problem", which suggests the existence of "exciton" in the SWNTs. In 2005, more directly, the two-photon absorption spectroscopy was carried out to determine the exciton binding energy [18, 19]. The huge exciton binding energy of hundred meV in the SWNTs was directly evaluated from the energy difference between 1s exciton PL and two-photon 2p exciton resonance peak [18, 19]. These experimental studies verified the existence of stable excitons in SWNTs, with huge binding energies on the order of several hundred meV [18–20]. The larger binding energy than the thermal energy at room temperature ($\approx$26 meV) indicates that the excitons in the SWNTs are stable even at room temperature. Moreover, noted that this exciton binding energy of several hundred meV in the SWNTs is much larger than that of several-tenth meV in the compound semiconductors. From these studies, it was found that the observed PL peak does not originate from free electron-hole pair recombination but instead from exciton recombination. This stable exciton dominates the optical properties including the optical dynamics and optical nonlinear response, even at room temperature.

2.1.6 Exciton Structures in Carbon Nanotubes

The one of the most striking features of SWNT electronic states are the two degenerate band structures at the K and K' valleys in momentum space [21]. Many configurations of the electron and hole forming the exciton are predicted due to the degeneracy of band structures. Here, the exciton configuration consists of an electron at the K valley and a hole at the K' valley, $|K; K'\rangle$, as shown in Fig. 2.7. Theoretical studies examining the exciton structure with respect to degenerate K and

Table 2.1 Table of exciton states due to the valley and spin degeneracy

| Spin	Valley	Degeneracy	Selection rule
singlet	$|K; K(+)\rangle$	1	○
	$|K; K'\rangle$	1	×
	$|K; K(-)\rangle$	1	×
	$|K'; K\rangle$	1	×
triplet	$|K; K(+)\rangle$	3	×
	$|K; K'\rangle$	3	×
	$|K; K(-)\rangle$	3	×
	$|K'; K\rangle$	3	×

K' valleys [15–17, 21], have indicated multiple exciton states, as shown in Table 2.1 [21]. The exciton states with zero angular momentum, $|K; K\rangle$ and $|K'; K'\rangle$, are split into bonding and anti-bonding exciton states due to the inter-valley (short-range) Coulomb interaction. The bonding state is odd parity, and the anti-bonding state is even parity. Exciton states are further classified by the singlet and triplet nature of the electron-hole spin configurations. The degree of band degeneracy and spin results in 16 exciton states, as shown in Table 2.1. The optical transition from only one exciton state, denoted as $|K; K(+)\rangle$, to the ground state is a dipole-allowed transition (singlet-bright exciton), dictated by the restriction of the optical selection rule (zero-momentum, singlet state, and odd parity). The other 15 exciton states are optically forbidden (dark excitons). These exciton structures dominate the optical properties of SWNTs, such as the exciton dynamics. Thus, the exciton fine structure, including the energy separation between the bright and dark exciton states, should be clarified experimentally.

2.2 Novel Excitonic Properties of Carbon Nanotube

2.2.1 Single Carbon Nanotube Spectroscopy for Revealing Exciton Structures

Figure 2.8 shows the typical macroscopic (ensemble averaged) PL spectrum from micelle encapsulated SWNTs in D_2O solution, indicated by the black line. The many PL peaks arising from various types of SWNTs with different chirarities (n, m) are observed in the ensemble averaged PL spectrum. The optically excited electron-hole pair in SWNTs forms the exciton state due to strong Coulomb interaction described in Sect. 2.1, and recombination of exciton is the origin of the PL signals in the SWNTs. The shape of ensemble averaged PL spectrum shows the near Gaussian function, which means that each SWNT with same chiral indices is in the different environment (local strain, dielectric constant, and . . .). The optical transition (absorption and PL) of each SWNT is affected from the Gaussian

Fig. 2.8 Ensemble-averaged PL spectrum (*black solid line*) and PL spectrum of a single SWNT (*gray solid line*)
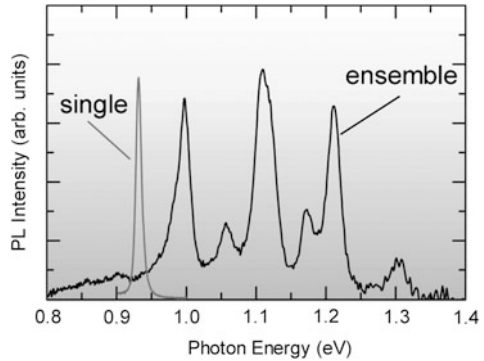

distributed inhomogeneous environment, causes fluctuation of the transition energy and broadens the optical spectrum. The PL broadening arising from the different environment is called as "inhomogeneous broadening", which covers the intrinsic optical properties of SWNTs. In contrast, the effect of the inhomogeneous broadening is eliminated in the PL spectra from a single SWNT. The sophisticated optical spectroscopic technique, called as a single carbon nanotube spectroscopy, enables us to reveal the exciton fine structures [22–26]. Figure 2.8 also shows the PL spectrum from a single SWNT, and the PL of a single SWNT shows very clear single peak and very narrow linewidth, which provide us the fruitful information on the excitonic properties of SWNT.

The samples used for single SWNT spectroscopy were isolated SWNTs synthesized on patterned Si substrates by an alcohol catalytic chemical vapor deposition method [27]. The Si substrates were patterned with parallel grooves typically from 300 nm to a few μm in width and 500 nm in depth using an electron-beam lithography technique. The isolated SWNTs grow from one side toward the opposite side of the groove. We prepared several SWNT samples by changing the growth temperature (650–850 °C) and time (30 sec–10 min). The average number density of isolated SWNTs in the sample is 0.1–1 μm^{-2}. Single SWNT PL measurements were carried out from 300 (room temperature) to 5 K using a home-built variable temperature confocal microscope setup. The SWNT samples mounted on a stage were excited with a continuous-wave He-Ne, and femtosecond pulsed Ti:Al$_2$O$_3$ laser, and the laser beam was focused on the sample surface through a microscope objective (NA 0.8). The PL signal from SWNTs was spectrally dispersed by a 30-cm spectrometer equipped with a liquid-nitrogen (LN$_2$)-cooled InGaAs photodiode array (spectral range: 0.78–1.38 eV), and CCD camera (>1.22 eV). The spectral resolution of the system was typically less than 0.7 meV. We also obtained PL images of the luminescent SWNTs on the sample, using a Si avalanche photodiode or electron multiple (EM) CCD camera.

Figure 2.9 shows a typical PL image of isolated semiconducting SWNTs at room temperature. The monitored PL energy range is typically between 1.18 and 1.37 eV. Several spatially isolated bright spots can be observed in the 3D image. Each bright spot represents the PL signal from a single luminescent SWNT because the PL spectrum obtained just on each bright spot has only a single PL peak [26].

Fig. 2.9 Three-dimensional
plots of the PL image of a
SWNT at room temperature
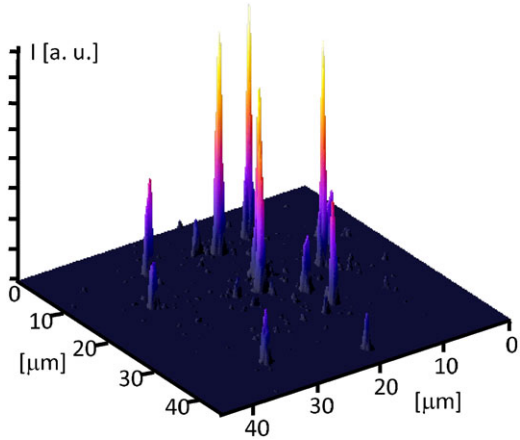
2.2.2 Singlet-Bright and -Dark Exciton Revealed by Magneto-PL Spectroscopy

Magneto optical spectroscopy is a versatile tool in order to study the exciton struc-
tures [28–33]. Here, we described low temperature magneto-PL spectroscopy of
single SWNT to study the singlet exciton structures with odd $|K; K(+)\rangle$ and even
$|K; K(-)\rangle$ parity due to the inter-valley Coulomb interaction [32]. In the magneto-
PL measurements of a 1D SWNTs, relative angle relationship between the nan-
otube and magnetic field (magnetic flux) should be characterized. Magneto-PL spec-
troscopy was carried out under Voigt and Faraday geometry. In the Voigt geometry,
in which laser light propagates perpendicular to the magnetic field, we can investi-
gate the effect of the magnetic flux threading the nanotube axis, while in the Faraday
geometry, in which the laser propagates parallel to the field, the magnetic flux is per-
pendicular to the tube axis.

Figure 2.10(a) shows the normalized PL spectra of a single (9,4) carbon nanotube
under a magnetic field in the Voigt geometry, where the relative angle α between the
tube axis and magnetic field is $\approx 9°$. A single and sharp PL spectrum arising from
bright exciton recombination is observed at zero magnetic field, and the shape of
PL spectrum from a single SWNT is approximated by a Lorentzian function, re-
flects homogeneous broadening [34–36]. This single and sharp spectrum of a single
carbon nanotube enables us to observe the spectral changes in detail, even under a
magnetic field of several T. An additional peak is clearly observed below the bright
exciton peak with an increasing field in Fig. 2.10(a). These PL spectra are fit well by
summation of two Lorentzian functions and the energy positions of the two peaks
can be evaluated accurately. The lower energy peak shows a redshift and the in-
tensity relative to the higher peak increases with the magnetic field. In contrast,
Fig. 2.10(b) shows the results of similar experiments on a single (9,5) nanotube per-
formed in the Faraday geometry, where the magnetic flux is perpendicular to the
nanotube axis. No spectral splitting induced by the magnetic field is observed in the

Fig. 2.10 Low temperature
of PL spectra of single
SWNT under a magnetic
field; (**a**) Voigt (B//z) and
(**b**) Faraday (B//z)
configurations (Reprinted
with permission from [32].
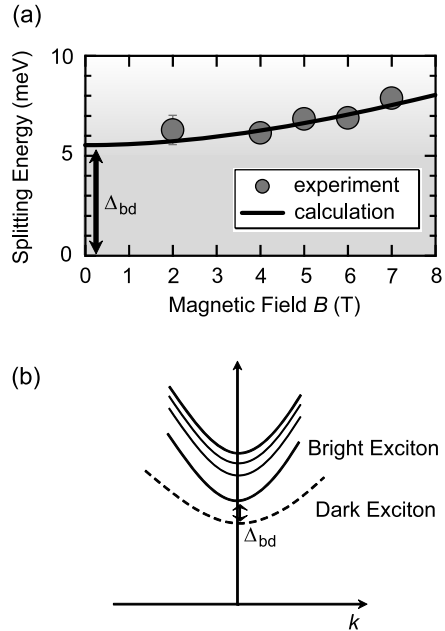Copyright, American
Physical Society)
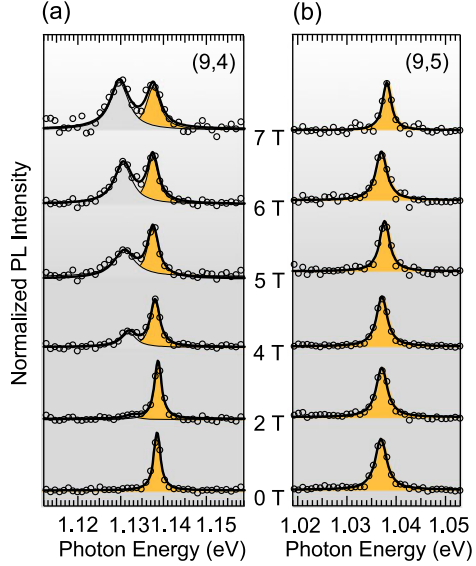
Faraday geometry, even under a magnetic field of 7 T. Note that the splitting of the
PL peak occurs due to the magnetic flux parallel to the nanotube axis.

Here, we discuss the experimentally observed change of PL spectrum induced by
the magnetic flux in a single carbon nanotube. The effective magnetic flux thread-
ing the nanotube is experimentally evaluated as $\phi = \pi d^2/4 \times B \cos\alpha$, where d is
the nanotube diameter and B is the strength of the magnetic field. According to
the theoretical calculation by Ajiki and Ando [37], the degenerated band-gaps in
semiconducting carbon nanotubes at the K and K' valleys are lifted due to the
Aharonov-Bohm effect. The split between the two states, Δ_{AB}, is described by

$$\Delta_{AB} = 6E_g\phi/\phi_0 \quad (\phi/\phi_0 < 1/6), \tag{2.4}$$

where $\phi_0 = ch/e$ is the magnetic quantum and E_g is the band-gap energy of the car-
bon nanotubes. In the excitonic picture with consideration of Coulomb interactions,
two degenerated valleys create four singlet exciton states, $|K; K\rangle, |K; K'\rangle, |K'; K\rangle$,
$|K'; K'\rangle$, where $|K; K\rangle$ means that the exciton consists of an electron (hole) in the K
(K) valley [21]. Moreover, the singlet exciton states with zero angular momentum,
$|K; K\rangle$ and $|K'; K'\rangle$, split into the bonding $|K; K(+)\rangle$ exciton state with odd parity
and antibonding $|K; K(-)\rangle$ exciton states with even parity due to the short-range
Coulomb interaction. The optical transition from $|K; K(+)\rangle$ ($|K; K(-)\rangle$) exciton
to the ground state is dipole allowed (forbidden) and $|K; K(+)\rangle$ ($|K; K(-)\rangle$) exci-
ton becomes bright (dark) state [21]. When the magnetic flux threads the nanotube
axis, the exciton states at the K and K' valleys become independent of each other,
and the singlet dark state with even parity gradually brightens as the magnetic field

(a)

(b)

is increased. Using Eq. (2.4), the energy difference $\Delta_{bd}(B)$ between the bright and dark exciton states under magnetic field B can be described by

$$\Delta_{AB}(B) = \sqrt{\Delta_{bd}^2 + \Delta_{AB}^2}, \tag{2.5}$$

where Δ_{bd} is the energy splitting at zero magnetic field [21].

Figure 2.11(a) shows the bright and dark exciton energies estimated from the Lorentzian spectra fitting procedure as a function of magnetic field. For the evaluation of Δ_{bd}, we assumed that the Aharonov-Bohm splitting is proportional to the magnetic flux, that is, $\Delta_{AB} = \mu\phi$, where μ is a constant [21]. Figure 2.11(a) shows the experimentally observed splitting values and the theoretical curve based on Eq. (2.5) where Δ_{bd} and μ are fitting parameters. The theoretically calculated curves reproduce the experimental results well. Here the value of Δ_{bd} is about 5.5 meV under zero magnetic field and the parameter μ is 1.14 meV/T nm^2 [32]. This result indicates that the singlet dark exciton state exists about 5.5 meV below the singlet bright exciton state in the (9,4) SWNT. The Aharonov-Bohm splitting of SWNTs with various chiral indices were experimentally observed [32]. We found that the singlet dark exciton states always lie at the lower energy side of singlet-bright exciton on order of a few meV, and its energy splitting strongly depends on the tube diameter.

Fig. 2.12 (**a**) PLE contour
map of a single (9,4) carbon
nanotube. The *arrow* shows
the weak satellite PL peak far
below the bright exciton PL
peak. (**b**) Temperature-
dependent PLspectra of a
single (7,5) carbon nanotube.
The *inset* shows the
temperature dependence of
the PL intensity ratio of the
satellite peak to the bright
exciton peak.PL spectra of
single SWNT with different
chiral index (*n*, *m*) (Reprinted
with permission from [43].
Copyright, American
Physical Society)
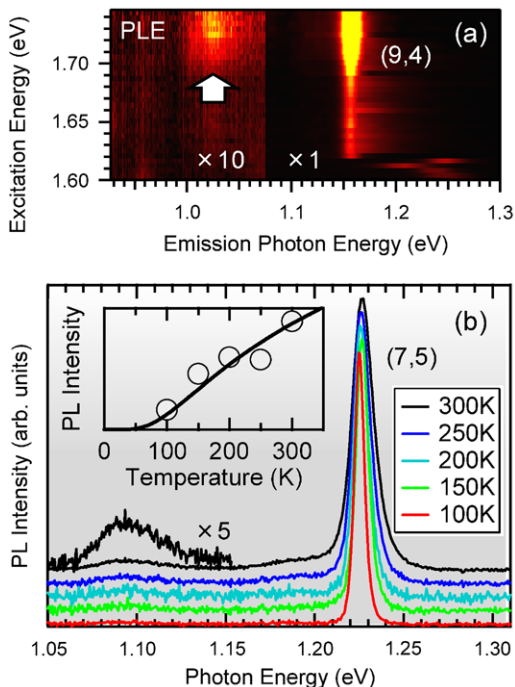
2.2.3 Triplet and *K*-Momentum Dark Exciton States

Recently, satellite PL peaks have been experimentally observed, with much lower
energies than the singlet bright exciton peak [38–42]. Since the lower exciton states
have considerable influence on the optical properties of carbon nanotubes, the origin
of the low-energy PL peaks has been a matter of intense debate. Here we describe the
low energy PL peaks arising from the triplet and *K*-momentum dark exciton states
in SWNTs [43]. Figure 2.12(a) shows a typical contour map of PLE for a single
(9,4) carbon nanotube with E_{11} singlet bright exciton peak at room temperature.

A sharp PL spectrum of a single SWNT provides a clear feature of the low-energy
PL band below the singlet bright exciton peak. We can observe a weak low-energy
PL peak ≈130 meV below the singlet bright exciton peak as indicated by the arrow
in Fig. 2.12(a), arising from the same (9,4) nanotube.

Figure 2.12(b) shows the temperature dependence of PL spectra of a single (7,5)
carbon nanotube, where each PL spectrum was normalized by the bright exciton
peak intensity. With decreasing temperature, the PL intensity of the weak low-
energy peak decreases. The ratio of the weak low-energy PL peak to the bright
exciton peak is shown in the inset of Fig. 2.12(b) as a function of temperature.
The characteristics behavior of decrease of this ratio with decreasing temperature
shows that the low-energy PL peak does not come from the lower dark exciton
states because the exciton population in the lower exciton states should increase and
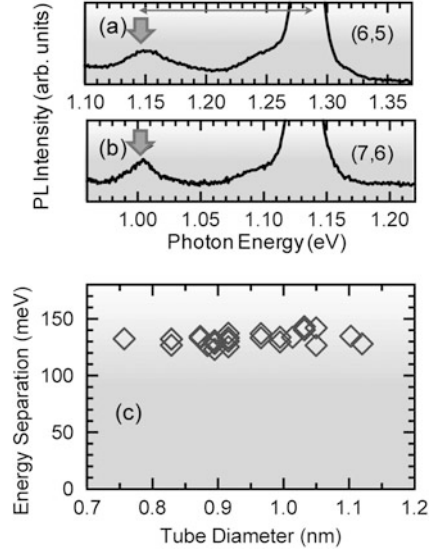
PL intensity is expected to increase at lower temperature. To evaluate the experimental data, we assumed that the low-energy peak is the phonon sideband of the K-momentum dark exciton states ($|K; K'\rangle$), emitting an in-plane TO (iTO) phonon at K-point [39, 40]. The temperature dependence of the PL intensity ratio of the phonon sideband I_{phonon} to the bright exciton state I_{bright} can be expressed as the product of the Boltzmann factor and the probability of emitting a phonon, i.e.,

$$\frac{I_{phonon}}{I_{bright}} \propto \exp\left(\frac{\Delta_K}{k_B T}\right) \times (n_{ph} + 1), \tag{2.6}$$

where Δ_K is the energy separation between the K-momentum dark and the bright exciton states, $n_{ph} = 1/[\exp(\Delta_{ph}/k_B T) - 1]$ is the phonon occupation number, and Δ_{ph} is the phonon energy. The solid curve in the inset of Fig. 2.12(b) shows the calculated result from Eq. (2.6) using $\Delta_K = 40$ meV and $\Delta_{ph} = 170$ meV and reproduces the experimental data well. These values are consistent with theoretical [14] and experimental studies [40, 44] on the phonon-mediated absorption peak ≈ 200 meV ($\approx \Delta_K + \Delta_{ph}$) above the bright exciton peak due to the K-momentum excitons. This result shows that the temperature dependence of the weak low-energy PL peak can be explained by considering the phonon sideband of the K-momentum dark exciton states.

We investigated the low-energy PL peak for many single carbon nanotubes with different chiralities shown in Figs. 2.13(a) and (b). In Fig. 2.13(c), we plotted the energy separation, Δ_1, between the weak low-energy PL peak and the bright exciton PL peak as a function of the tube diameter. Although some of the data are slightly scattered even in the same-chirality tubes, this result indicates that $\Delta_1 = \Delta_{ph} - \Delta_K$ is about 130 meV and almost independent of the tube diameter. This is consistent with the considerations of the phonon sideband discussed above because the energy

Fig. 2.14 (**a**) PL spectra of a single (12,1) carbon nanotube before and after pulsed-laser irradiation. (**b**) Temperature dependence of PL spectra of a single (8,7) carbon nanotube after pulsed-laser irradiation (Reprinted with permission from [43]. Copyright, American Physical Society)
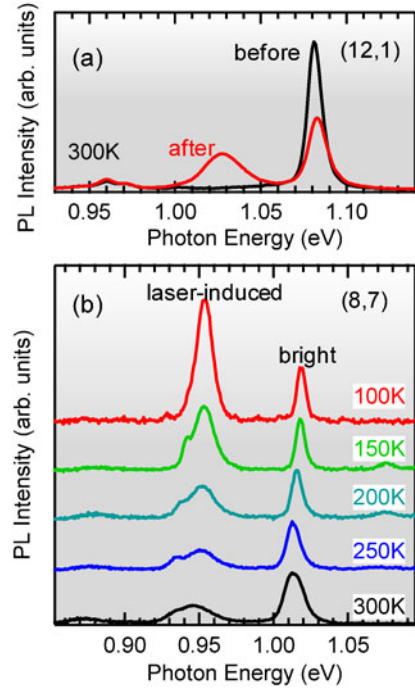

of the iTO phonon mode, Δ_{ph}, is dominant in Δ_1, and almost independent of the tube diameter within the diameter range shown in Fig. 2.13(c). The both the temperature and diameter dependences of the weak low-energy PL peak strongly indicate that it arises from the phonon sideband of the K-momentum dark exciton states. Therefore, from these results, it was found that K-momentum dark exciton states lie above the singlet-bright exciton states above 40 meV.

Here, we also investigated the effect of the pulsed-laser irradiation to single carbon nanotubes, since the strong pulsed-laser irradiation has been reported to induce the appearance of a low-energy PL peak [41, 43]. We irradiated the femtosecond pulsed-laser with 735-nm wavelength and ≈2 mW to single carbon nanotubes. Figure 2.14(a) shows PL spectra of a single (12,1) carbon nanotube before/after the pulse irradiation, respectively. Additional satellite PL peak appears 70 meV below the bright exciton peak. Moreover, we also observed the weak phonon sideband simultaneously discussed above 130 meV below the bright peak.

Figure 2.15(b) shows temperature dependence of the PL spectra for an (8,7) carbon nanotube after pulsed-laser irradiation. As temperature decreases, we observed that the intensity of the low-energy PL peak induced by the laser irradiation increases, in contrast with the phonon sideband at 0.87 eV, which decreases at low temperatures. This result clearly shows that the origin of the laser-induced PL peak is completely different from the phonon sideband of the K-momentum dark exciton states and that some light-emitting states lie at much lower energies than the singlet bright exciton state.

Fig. 2.15 (**a**) and (**b**) PL
spectra of single (7,5) and
(9,4) carbon nanotubes,
respectively, before and after
laser irradiation.
(**c**) Tube-diameter
dependence of the energy
separation between the bright
exciton and the strong
low-energy peak induced by
the laser irradiation. The
curve shows a fit with the
splitting energy proportional
to $1/d^2$ (Reprinted with
permission from [43].
Copyright, American
Physical Society)
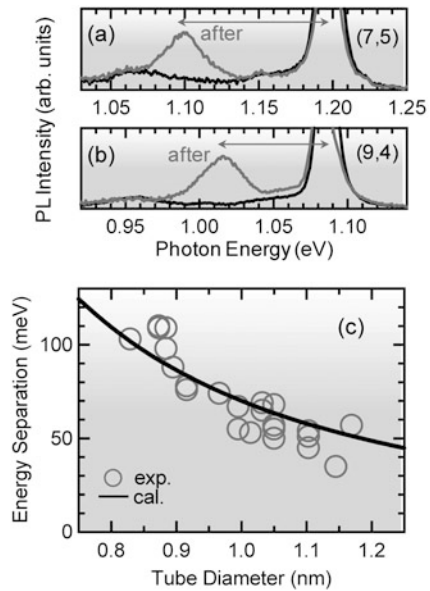
We investigated the laser-induced low-energy PL peak for many carbon nan-
otubes, as typically shown in Figs. 2.15(a) and (b), and plotted the separation en-
ergy Δ_2 between the bright exciton peak and the laser-induced peak in Fig. 2.15(c).
The experimental results show that Δ_2 strongly depends on the tube diameter, with
a smaller-diameter tube having a larger Δ_2. We fit the data to $\Delta_2 = A/d^2$, where
A is a coefficient and d is the tube diameter, as shown in Fig. 2.15(c), which re-
produces the experimental results with $A \approx 70$ meV nm^2. Capaz *et al.* theoretically
predicted that the tube-diameter dependence of the splitting energy between the sin-
glet and triplet exciton states is proportional to $1/d^2$ because of the tube-diameter-
dependent exchange interaction [45, 46]. The calculated proportionality coefficient
is ≈ 40 meV nm^2 for the micelle-wrapped SWNTs with a relative dielectric constant,
ϵ, of ≈ 3 [47]. However, the value of proportionality coefficient ($A \approx 70$ meV nm^2)
can be well accounted with consideration of smaller dielectric constant $\epsilon \approx 1.8$ in
this air-suspended SWNTs. This suggests that the origin of the laser-induced low-
energy PL peak is the triplet dark exciton states. Although the spin-orbit interaction
is small in carbon nanotubes and graphene due to a small mass of the carbon atoms,
a recent theoretical study showed that impurities on graphene lead to a large in-
crease of the spin-orbit coupling [48–50]. Therefore, we believe that defects created
by the laser irradiation, or any impurities trapped by the defects, would result in an
increase in the spin-orbit coupling, leading to the spin-flip process and PL from the
triplet exciton states.

Fig. 2.16 PLE contour maps of (**a**) nondoped CoMoCAT-PFO nanotubes, (**b**) CoMoCAT-PFO nanotubes doped with F_4TCNQ solutions. The *dotted circles* show the E_{11} bright excitons and the *solid circles* show the new PL peaks due to hole doping. (**c**) The normalized PL spectra of the nondoped and doped CoMoCAT-PFO nanotubes [from (**a**) and (**b**), respectively] at the excitation photon energy of 1.9 eV. The doping-induced new PL peaks of (7,5) and (7,6) nanotubes are indicated by the *solid* and *open arrows*, respectively (Reprinted with permission from [51]. Copyright, American Physical Society)
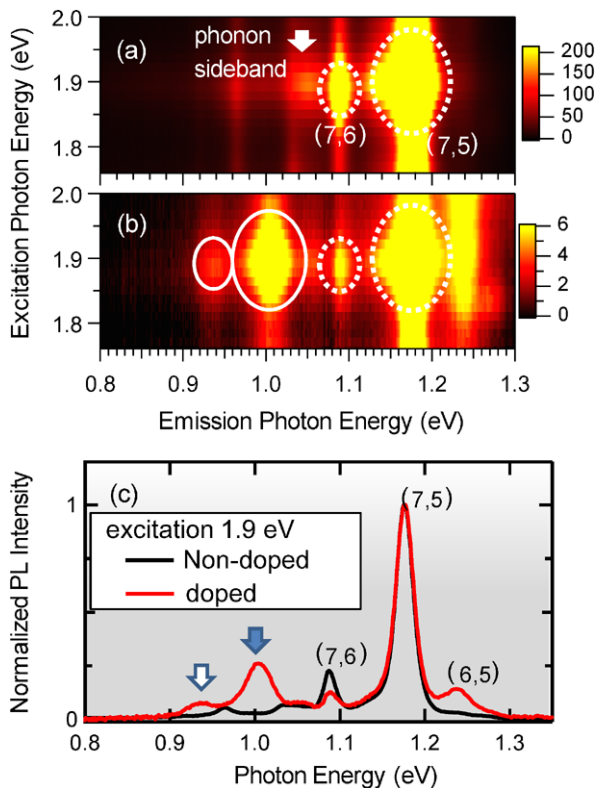
2.2.4 Exciton-Complex in Carbon Nanotubes

Despite the importance of many particle bound states such as exciton-exciton or exciton-electron (hole) complexes, the many particle bound states in carbon nanotubes are not yet fully understood. Here, we describe the many-particle bound states (exciton-complex) in hole-doped single-walled carbon nanotubes [51]. Figure 2.16(a) shows a contour map of PLE for non-carrier doped CoMoCAT nanotube dispersed by poly[9,9-dioctylfluorenyl-2,7-diyl] (CoMoCAT-PFO) in a toluene solution, which included many (7,5) nanotubes and a small amount of (7,6) nanotubes [52]. The dotted circles in Fig. 2.16(a) indicate the PL of the E_{11} singlet bright excitons in the (7,5) and (7,6) nanotubes. The side peak indicated by the arrow in Fig. 2.16(a) is the phonon sideband of the K-momentum dark excitons in (7,5) carbon nanotubes as described in 3-3. Figure 2.16(b) shows the PLE map after a p-type (hole) doping with 2,3,5,6-tetrafluoro-7,7,8,8-tetracyanoquinodimethane (F_4TCNQ). At the lower energy side of singlet exciton peak, new PL peaks appears, as indicated by the solid circles in Fig. 2.16(b). These PL peaks are clearly associated with (7,5) and (7,6) carbon nanotubes. Figure 2.16(c) shows the normalized PL spectra of the non-doped and doped CoMoCAT-PFO nanotubes (Figs. 2.16(a)

Fig. 2.17 (**a**) The hole-doping dependence of the absorption spectra of CoMoCAT-PFO nanotubes. The *inset* shows an enlarged view of the lower-energy region where the new peaks appear. The new peaks indicated by the arrows A and B are associated with (7,5) and (7,6) nanotubes, respectively. (**b**) The hole-doping dependence of the absorption intensity of the E_{11} bright excitons (*left axis*) and the new peak (*right axis*) of (7,5) carbon nanotubes (Reprinted with permission from [51]. Copyright, American Physical Society)
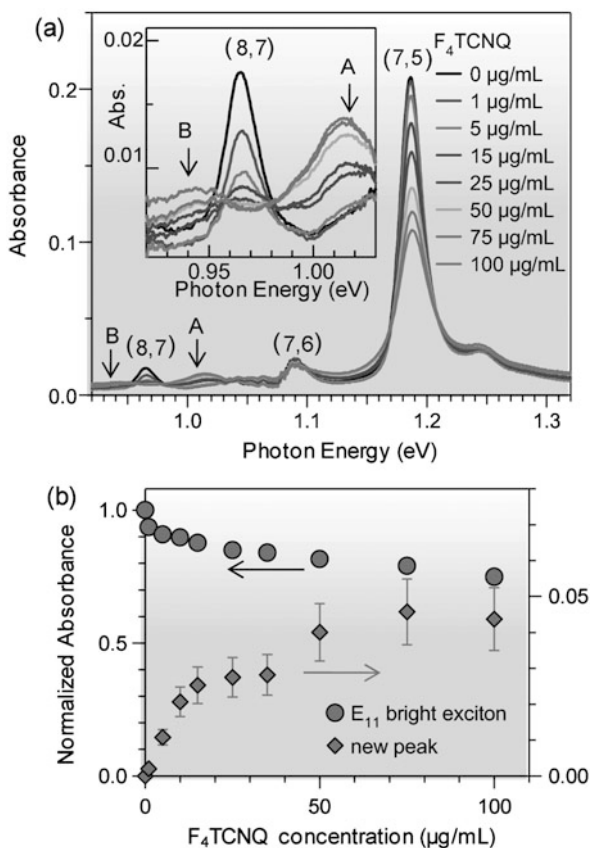
and (b), respectively) at the excitation photon energy of 1.9 eV. The doping-induced new PL peaks are indicated by the arrows in Fig. 2.16(c).

Figure 2.17(a) shows the absorption spectra of CoMoCAT-PFO nanotubes with F_4TCNQ solutions added. The inset shows an enlarged view of the low-energy side. With increasing F_4TCNQ concentration, the new absorption peaks appears as indicated by the arrows A and B in Fig. 2.17(a). Compared with the new PL peaks observed in Fig. 2.17(a), we found that the absorption peaks A and B are associated with (7,5) and (7,6) nanotubes, respectively. Figure 2.17(b) shows the normalized absorption intensity of the singlet bright exciton peak (left axis) and the new peak (right axis) of (7,5) carbon nanotubes as a function of F_4TCNQ concentration. While the absorption intensity of the bright exciton decreases due to the hole-doping [53], the absorbance of the new state increases. In the same way, we also performed hole-doping to HiPco-PFO nanotubes by adding F_4TCNQ and HiPco-SDBS (SDBS: sodium dodecylbenzene sulfonate) nanotubes by adding AB (4-amino-1,1-azobenzene-3,4-disulphonic acid) solutions. Note that we observed the appearance of the same new PL and absorption peaks in the SWNTs samples with using different dispersing agents and dopant molecules. These results indicate
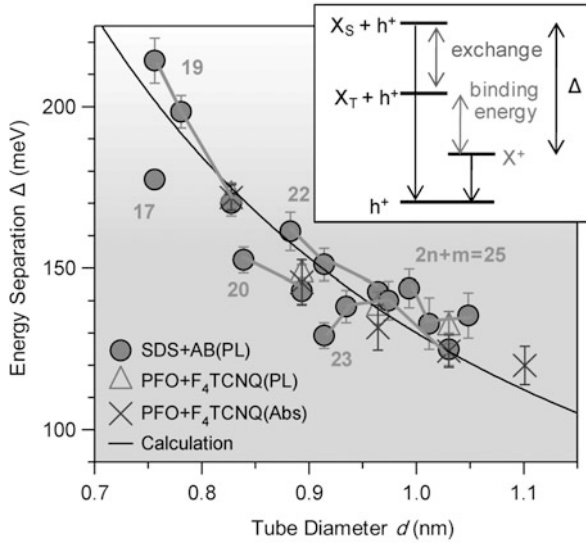
Fig. 2.18 Tube diameter d dependence of the energy separation between the bright exciton state and the new state observed in PL and absorption spectra. The *green numbers* show the value of $2n + m$ for (n, m) nanotubes. The calculated *solid curve* shows the sum of the exchange splitting of $70/d^2$ meV and the trion binding energy of $60/d$ meV. *Inset* shows the schematic of the energy levels of the singlet and triplet excitons (X_S and X_T) and the trions (X^+). A free hole is denoted as h^+ (Reprinted with permission from [51]. Copyright, American Physical Society)

that the new PL peak observed in hole-doped carbon nanotubes is independent of the dopant species, and that the new state exhibits intrinsic properties of hole-doped carbon nanotubes, rather than any chemical complex with a specific dopant.

Figure 2.18 shows the tube-diameter dependence of the energy separation Δ between the bright exciton state and the new state observed in the PL and absorption spectra. The energy separation depends strongly on the tube diameter, but not on the species of dopants. The value of Δ is about 130 meV for 1-nm diameter. This diameter dependence of the new peak is completely different from the phonon sideband of the K-momentum dark excitons or the luminescence of triplet excitons, as described in Sects. 2.2 and 2.3. The new PL and absorption peaks appear with very small Stokes shifts. In Fig. 2.18, we also show the value of $2n + m$ for each chirality with the HiPco-SDS data, where (n, m) is the chiral index. The HiPco-SDS data show clear family patterns, which are well-known optical characteristics of carbon nanotubes, similar to the exciton binding energy [46]. This result confirmed that the new state arises from the intrinsic properties of carrier-doped carbon nanotubes, rather than specific dopants.

Here, we consider the origin of the intrinsic low-energy PL and absorption peaks. Theoretical calculations have shown that stable trions (charged excitons) can exist in carbon nanotubes [54–56]. A trion binding energy is defined as the energy required for dissociating a trion into a free hole and an exciton. The calculated trion binding energy in carbon nanotubes for dielectric constant of 3.5 is about $40/d$ meV,

where d is the tube diameter (n, m), and is much larger than that in other II–VI or III–V compound semiconductors. It means that trions in carbon nanotubes are detectable even at room temperature [51, 57]. Thus, we assign the new state below the singlet excitons in hole-doped carbon nanotubes to trions, which have not been experimentally reported in carbon nanotubes so far [53].

The energy separation between the bright excitons and trions observed in our experiments for 1-nm-diameter tube was about 130 meV, which is very large value. We attribute the extremely large energy separation to the electron-hole exchange interaction originating from the short-range Coulomb interaction in carbon nanotubes, which has not been considered in the previous trion calculations [50]. The excitons in carbon nanotubes have large singlet-triplet splitting as much as several tens of meV, as described in Sects. 2.2 and 2.3. This is because the strong exchange interaction between an electron and a hole in carbon nanotubes significantly lifts up the energy level of the singlet bright exciton state. Thus, the trion binding energy corresponds to the energy separation between the trion states and the lowest triplet exciton states, as shown in the inset of Fig. 2.18. Assuming the trion binding energy of $\approx 60/d$ meV and the singlet-triplet exciton splitting of $70/d^2$ meV [43], we show the energy separation $\Delta = 70/d^2 + 60/d$ as the solid curve in Fig. 2.18. The solid curve is in good agreement with the experimental data. Thus, we concluded that the trion can be stable in hole-doped carbon nanotubes even at room temperature.

2.3 Novel Exciton Dynamics of Carbon Nanotube

2.3.1 Exciton Relaxation Dynamics Between Bright and Dark State

The exciton dynamics are important issues, which leads to the understanding of the novel excitonic properties of carbon nanotube. Here, we studied the exciton relaxation and distribution between the bright and dark states through the magnetic- and temperature-dependences of the PL spectra of single carbon nanotubes.

Figure 2.19(a) shows the temperature dependence of the magneto-PL spectra for a (7,5) nanotube in a 7 T field [58]. The two PL peaks from the dark and bright exciton states are observed, as in Fig. 2.10(a). The PL peak from the dark exciton state at the lower energy side is more clearly observed at lower temperatures. This result can be explained by the concentrating of the population in the lower dark exciton state with decreasing temperature, as the PL intensity can be represented as the product of the oscillator strength and the population of excitons.

We investigated the exciton population from the PL intensity ratio of the dark to the bright excitons, I_d/I_b. We also checked the magneto-PL spectra at various excitation laser powers, as shown in Fig. 2.19(b) and confirmed that I_d/I_b was independent of the laser power in our weak excitation conditions in Fig. 2.19(c). Figure 2.20(a) shows the temperature dependence of I_d/I_b at a magnetic field of 7 T for the (7,5) carbon nanotube shown in Fig. 2.19(a). We therefore concluded that heating of the nanotubes due to excitation laser could be neglected. While I_d/I_b (solid

Fig. 2.19 (**a**) Temperature-dependence of magneto-PL spectra at 7 T for a single (7,5) nanotube. (**b**) Magneto-PL spectra at 7 T for a (7,6) carbon nanotube under various excitation laser powers. (**c**) Laser-power dependence of the PL intensity ratio of the dark to the bright excitons in the (**b**) (Reprinted with permission from [58]. Copyright, American Physical Society)
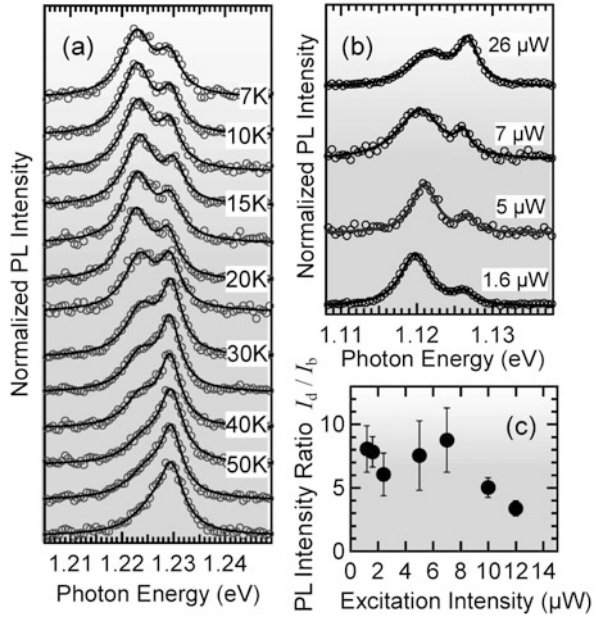

Fig. 2.20 (**a**) Temperature dependence of the PL intensity ratio of the dark to the bright excitons at 7 T for the (7,5) nanotube. *Solid circles* show experimental results and the lines indicate the calculated results for each Γ_d/γ_0. (**b**) Temperature dependence of Γ_d/γ_0 evaluated from (**a**). *Inset*: Schematic of a three-level model, with the bright and dark exciton states and a ground state (Reprinted with permission from [58]. Copyright, American Physical Society)
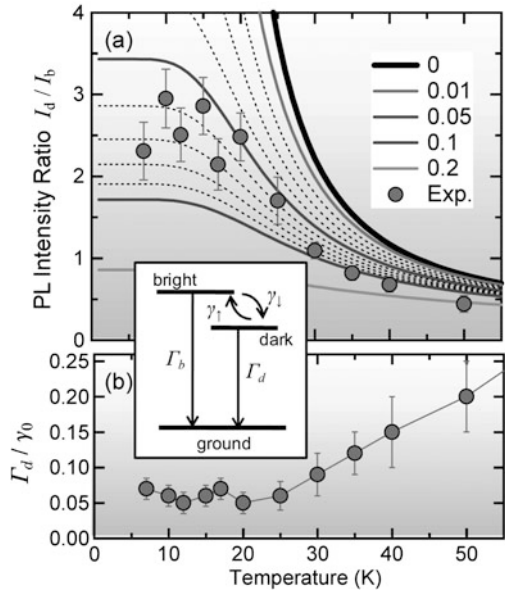
circles) in Fig. 2.19(b) increases with decreasing temperature, it clearly saturates below 20 K. In a Boltzmann exciton distribution, I_d/I_b should diversely increase toward low temperatures (the thick solid black line in Fig. 2.20(a)) because the exci-

ton population fully concentrates on the lower dark state. However, the experimental data do not diverge as rapidly as expected for a Boltzmann distribution.

We consider the transition rates between the bright and dark exciton states at 7 T to understand the experimental results. Inset of Fig. 2.20 shows a schematic of a three-level model consisting of bright and dark exciton states with a splitting energy Δ_{bd} and a ground state [59]. The lifetimes of the bright and dark excitons are denoted as $1/\Gamma_b$ and $1/\Gamma_d$, respectively. The $\gamma_{down} = \gamma_0(n+1)$ and $\gamma_{up} = \gamma_0 n$ represent the up and down scattering rate between the bright and dark exciton states through phonon emission and absorption processes, respectively, where $n = 1/[\exp(\Delta_{bd}/k_B T) - 1]$ is the phonon occupation number and γ_0 is the temperature-independent scattering rate. The rate equation for the dark exciton population can be expressed as

$$\frac{dN_d}{dt} = \gamma_{down} N_b - (\gamma_{up} + \Gamma_d) N_d, \tag{2.7}$$

where N_b and N_d are the populations of the bright and dark exciton states, respectively. In the steady state ($dN_d/dt = 0$), the population ratio of the dark to the bright exciton state is

$$\frac{N_d}{N_b} = \frac{\exp(\Delta/k_B T)}{1 + \frac{\Gamma_d}{\gamma_0}(\exp(\Delta/k_B T) - 1)}. \tag{2.8}$$

This equation indicates that N_d/N_b depends on the term Γ_d/γ_0, the ratio of the dark exciton lifetime to the thermalization time between the two exciton states. If the phonon-induced exciton scattering rate γ_0 is large enough, the ratio can be neglected ($\Gamma_d/\gamma_0 \to 0$) and N_d/N_b simplifies to $\exp(\Delta/k_B T)$, a Boltzmann distribution. The thick solid black line in Fig. 2.20 shows the calculated I_d/I_b, assuming the Boltzmann distribution between the bright and dark exciton states. Here, according to the expression given in Ref. [30], we calculated the relative oscillator strength of the dark to the bright excitons at 7 T as ≈ 0.17. The other lines correspond to the calculated results for each value of Γ_d/γ_0. Below 20 K, the calculated line for $\Gamma_d/\gamma_0 = 0.06 \pm 0.02$ reproduces the experimental data well.

We determined the values of Γ_d/γ_0 for each temperature from the experimental data, and plotted them as a function of temperature in Fig. 2.20(d). Since γ_0 is temperature-independent, we can determine the temperature dependence of the dark exciton decay rate Γ_d, which is dominated by the non-radiative process. The Γ_d is almost constant below about 20 K, and becomes large with increasing temperature. This dependence is similar to the reported bright exciton decay rate [59]. At room temperature, up to 7 T, we could hardly observe the dark exciton PL peak. Therefore we concluded that Γ_d/γ_0 is at least larger than 1 at room temperature at 7 T. A consistent result has been recently reported by using time-resolved spectroscopy for single nanotubes [60].

Our result suggests that the phonon-induced exciton scattering between the bright and dark states does not occur rapidly as compared to the dark exciton lifetime. This means that the excitons are not fully thermalized between the two states. Theory predicts that the phonon cannot scatter excitons between these two states for ideal

carbon nanotubes because the bright and dark excitons have odd and even parities, respectively, and the phonon cannot break the symmetry [61]. Therefore, the slow phonon-induced exciton scattering between the bright and dark states leading to the non-Boltzmann distribution can be explained by different parities of the two exciton states. It means that the phonon-induced exciton scattering time between the bright and dark exciton states cannot be neglected against the dark exciton lifetime, and that PL dynamics in carbon nanotubes is under the influence of the non-Boltzmann exciton distribution between the bright and dark states.

2.3.2 Radiative Lifetime of Bright Exciton States

The exciton spatial coherence volume (length) is defined as the volume from which the exciton can coherently capture the oscillator strength, and is an important parameter [62]. The exciton radiative lifetimes and the PL quantum yields (η) are therefore dominated by the coherence volumes (lengths) [62]. Moreover, the coherence lengths in SWNTs also determine whether the exciton motion can be treated as diffusive or not. This is directly related to the exciton relaxation mechanism and nonlinear optical properties. Here, we investigated the exciton radiative lifetimes of SWNTs using highly isolated SWNT ensembles with high PL quantum yields, and determined the exciton coherence lengths from the radiative lifetimes.

Figure 2.21(a) shows the absorption spectra of PFO-dispersed SWNTs and SDBS-dispersed SWNTs. The underlying background in the absorption spectrum of PFO-dispersed SWNTs is remarkably suppressed compared to that of the SDBS-dispersed SWNTs, and the absorption peaks are much more pronounced. This indicates that bundled SWNTs, residual impurities, or other amorphous and graphitic carbons were not included in the PFO-dispersed sample. Figure 2.21(b) shows the PLE map of PFO-dispersed SWNTs. The absorption spectra and PLE spectra show that only several types of chiral indices were included in the PFO-dispersed SWNTs samples. The diameters of SWNTs in the sample estimated from the absorption and PLE spectra range from $\approx$0.8 to 1.2 nm.

The η values of SWNTs were determined by comparison with those of the reference dyes (Styryl-13 and Rhodamine-6G). The η of Styryl-13 was calibrated against that of Rhodamine-6G in methanol ($\eta = 95$ %). In addition to the absorption spectrum with very low backgrounds, the small number of peaks enabled us to extract η of each (n, m) nanotube type in the PFO-dispersed sample. Figure 2.22(a) shows the absorption spectrum and the reconstructed spectrum based on the observed PLE spectrum. The reconstructed spectrum is the total of each (n, m) PLE spectrum, with only the amplitude of the peak varied as a fitting parameter. From the peak heights obtained in the fitting procedure, we determined the absorbance of each (n, m) peak at E_{22}. Figure 2.22(b) shows the evaluated η_{PL} of PFO-dispersed SWNTs as a function of tube diameter under the E_{22} resonance excitation conditions in each chiral index, where the relaxation rates from E_{22} to E_{11} were assumed to be independent
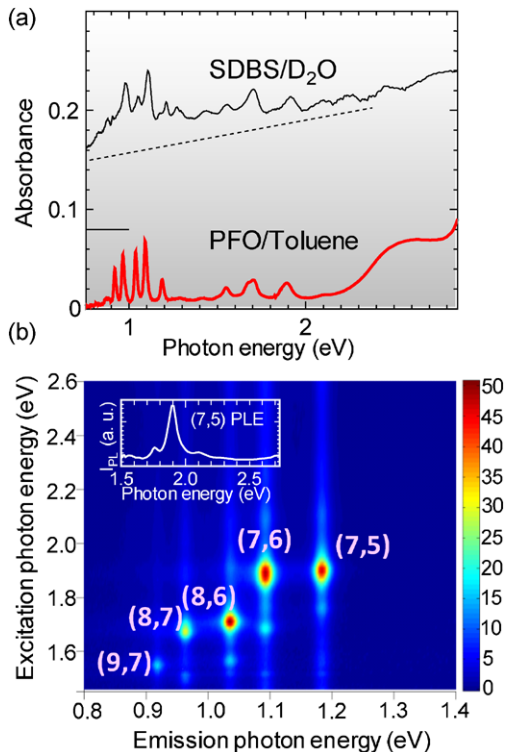
of the chirality [63]. We estimated the η_{PL} to be from $\approx$0.3 % to $\approx$1.6 %, depending on the tube diameter. The relatively smaller diameter nanotubes have larger η_{PL} values, reaching $\approx$1.6 % for (7,5) SWNTs.

We measured the PL lifetimes using the femtosecond excitation correlation (FEC) method. The FEC method has been successfully applied to a variety of materials, including SWNTs, to measure the recombination lifetimes of excitons [64, 65]. In the FEC experiments, the SWNTs were excited with optical pulses from a Ti:sapphire laser of central wavelength 745 nm, repetition rate 80 MHz, pulse duration $\approx$150 fs, and spectral width 8 nm. The two beams separated by the delay time were chopped at 800 and 670 Hz, respectively, and collinearly focused onto the same spot ($\approx$10 μm). Only the PL signal components modulated at the sum frequency (1470 Hz) were detected as FEC signals with a photomultiplier and a lock-in amplifier after dispersion of PL by a monochromator. The measurements were carried out under the excitation condition $\approx$100 μJ/cm^2. For a material with efficient exciton-exciton annihilation processes, FEC signal $I_C(\tau)$ for the delay time τ can be expressed as

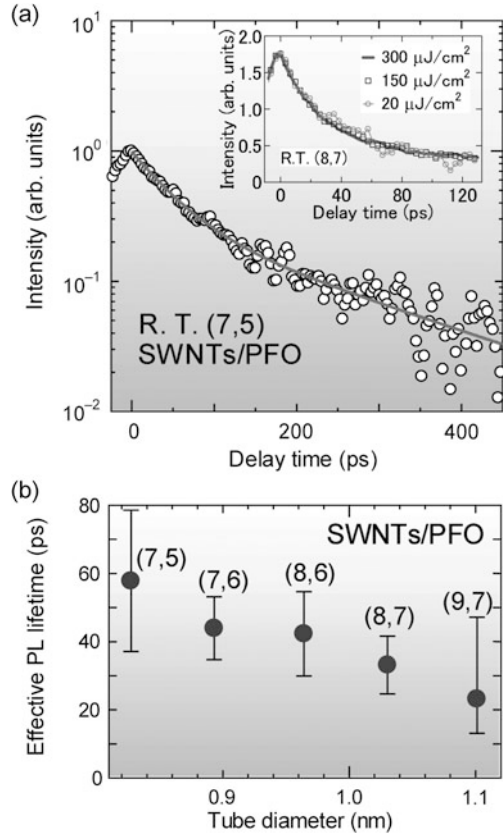$$I_C(\tau) \propto \int_0^\infty N_1(t)\, dt \qquad (2.9)$$
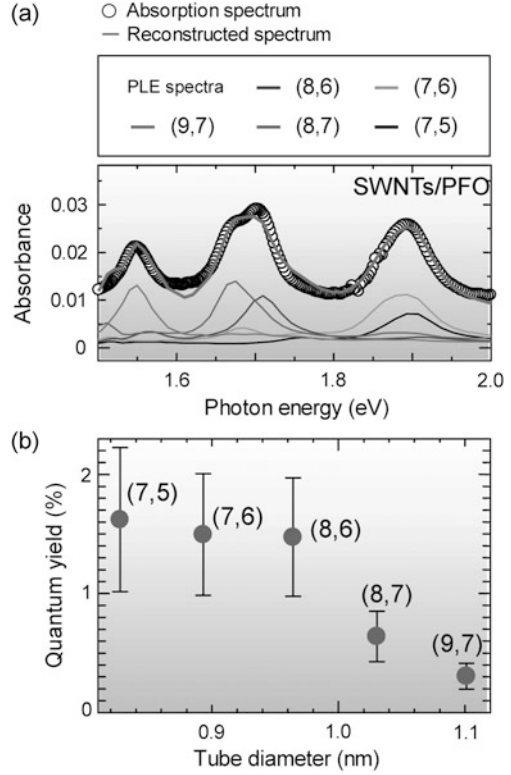
where $N_1(t)$ is the single exciton population decay. Since exciton-exciton annihilation processes occur efficiently in SWNTs [66], we are able to measure the PL lifetimes of SWNTs using the FEC technique. Detailed discussions on the PL lifetime measurement of SWNTs using FEC technique are presented in Ref. [65].

Figure 2.23(a) shows the FEC signals as a function of delay time for (7,5) SWNTs. The upward direction on the vertical axis indicates that the FEC signals have a negative sign. We checked that the FEC decay curves did not change by the excitation power density in the range from $\approx$20 to 300 μJ/cm^2 [see in inset of Fig. 2.23(a)]. The decay curve is closely described by a double exponential function (solid line) after subtracting the background signals. According to Eq. (2.9), the exciton population showing double exponential decay as $N_1(t) = C \exp(-t/\tau_A) + (1 - C) \exp(-t/\tau_B)(0 \leq C \leq 1, \tau_A < \tau_B)$ gives the FEC signal $I_C(\tau)$ as

$$I_C(\tau) \propto \left[C\tau_A \exp(-t/\tau_A) + (1 - C)\tau_B \exp(-t/\tau_B) \right] \qquad (2.10)$$

where C is the fractional amplitude of the fast decay component. Here, we define the effective PL lifetime as $\tau_{PL} = C\tau_A + (1 - C)\tau_B$, and the ratio of the fast component as $Y_A = C\tau_A/[C\tau_A + (1 - C)\tau_B]$. For (7,5) SWNTs in Fig. 2.23(a), we obtained $Y_A \approx 0.7$, $\tau_A \approx 45$ ps, and $\tau_B \approx 200$ ps by the fitting procedure. These are similar to the recently reported values for single (6,5) SWNTs in surfactant suspension

[67]. The effective PL lifetime τ_{PL} is calculated as ≈60 ps for (7,5) SWNTs. Figure 2.23(b) shows the effective PL lifetimes of PFO-dispersed SWNTs as a function of tube diameter. SWNTs with small diameters tended to have larger values.

Figure 2.24 shows the experimentally derived radiative lifetimes τ_R of SWNTs at room temperature as a function of tube diameter. The τ_R are calculated from η_{PL} in Fig. 2.22(b) and τ_{PL} in Fig. 2.23(b) as $\tau_R = \tau_{PL}/\eta_{PL}$. We found that the evaluated τ_R are typically ≈3–10 ns, and slightly increase with the tube diameter. From the obtained radiative lifetime at room temperature, the oscillator strength and the coherence length L_c of the 1D exciton states in SWNTs can be deduced. Note that the experimentally observed radiative decay rate τ_R^{-1} does not simply correspond to that of the bright $K_{ex} = 0$ exciton τ_0^{-1}, where K_{ex} is the exciton momentum. The oscillator strength of $K_{ex} = 0$ exciton is shared by all states within the finite homogeneous linewidth $\Gamma(T)$ due to the uncertainty of K_{ex} induced by dephasing process [68], and here we define the oscillator strength reduced by dephasing process as F_x. In addition, both the thermalization within each single exciton band, and the exciton distribution among bright and dark exciton states further reduce the F_x

Fig. 2.24 (**a**) Determined radiative lifetimes τ_R of SWNTs as a function of tube diameter. *Inset* shows deduced coherence lengths L_c as a function of tube diameter (Reprinted with permission from [52]. Copyright, American Physical Society)
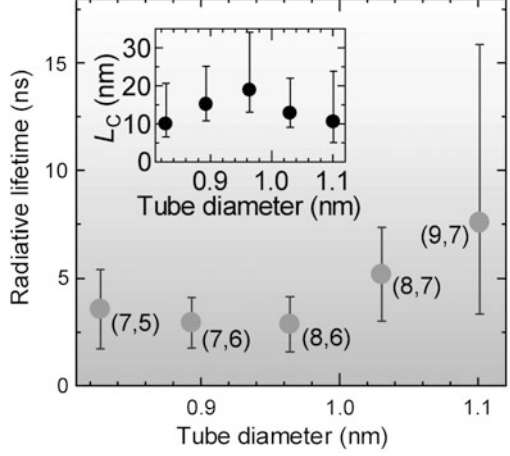
to the effective oscillator strength $F_{x,eff}$. We can obtain $F_{x,eff}$ from the measured τ_R as

$$F_{x,eff} = \frac{2\pi\epsilon_0 m_0\hbar^2 c^3}{\tau_R n e^2 E_x^2}, \tag{2.11}$$

where n is the refractive index (≈ 1.5 for toluene), m_0 is the electron mass, and E_x is the exciton energy.

The fraction of excitons $r_S(T)$ within $\Gamma(T)$ among the thermalized excitons in the bright exciton band can contribute to radiative recombination. $r_S(T)$ is given by [68]

$$r_S(T) = \int_0^{\Delta(T)} D(E)e^{-E/k_B T} dE \Big/ \int_0^\infty D(E)e^{-E/k_B T} dE, \tag{2.12}$$

where $D(E)$ is the exciton density of states. For the 1D case, assuming $D(E) \propto 1/\sqrt{E}$, we obtain $r_S(T) = \mathrm{erf}(\sqrt{\Gamma/k_B T}) \approx \sqrt{\Gamma/k_B T}$. The $T^{-1/2}$ dependence of the radiative decay rate has been observed in the temperature dependence in the PL measurements [31, 69]. As mentioned above, the exciton distribution between singlet bright and dark states decreases F_x again by a factor of [17]

$$r_M(T) = e^{-\delta_1 k_B T} \Big/ \left(1 + e^{-\Delta_{bd}/k_B T} + 2e^{-\Delta_K/k_B T}\right), \tag{2.13}$$

where Δ_{bd} and Δ_K are the energy differences of the bright exciton and higher dark excitons measured from the bottom of the lowest singlet dark exciton band, respectively. Since the relationship between $F_{x,eff}$ and F_x is expressed as $F_x = r_S^{-1} r_M^{-1} F_{x,eff}$ using $r_S(T)$ and $r_M(T)$, we thus determine the oscillator strength F_x from $F_{x,eff}$. Using experimentally obtained values of $\Delta(T) \approx 13$ meV for a single nanotube at room temperature [36], $\Delta_{bd} \approx 4$ meV [32] and $\Delta_K - \Delta_{bd} \approx 30$ meV [44], we obtain the factor $r_S^{-1}(T)r_M^{-1}(T)$ for (7,5) SWNTs.

The F_x contains information on the exciton coherence length. The exciton coherence length L_c and the exciton oscillator strength F_X are related as $L_c =$

$F_X/f_0|\phi(0)|^2$, where f_0 is the oscillator strength of a single k-state in the 1D momentum space, and $\phi(Z_e - Z_h)$ denotes the envelope function of the electron-hole relative motion. In the 1D case, $|\phi(0)|^2 \approx 1/a_X\sqrt{\pi}$, where a_X is the exciton Bohr radius (exciton size). Using the theoretical derived value of $a_X \approx 1.5$ nm [46] and evaluating $f_0 \approx 5$ according to Ref. [70], we evaluate the coherence length of excitons as $L_c \approx 10$ nm in (7,5) SWNTs.

Inset in Fig. 2.24 shows the evaluated coherence lengths for various (n, m) SWNTs. Here, we neglected the diameter dependence of $\Delta_K - \Delta_{bd}$ because of their small contribution. We found that each (n, m) type has similar values of $L_c \approx 10$ nm. These are in good agreement with the calculated values of L_c from the different formula using Γ and the exciton effective mass [71].

From our results, we can comment on the motion of excitons in SWNTs: The previously observed exciton excursion range of ≈ 100 nm [72, 73] is determined by the diffusive motion of the excitons because the $L_c \approx 10$ nm is much smaller than the diffusion length. The L_c also gives the saturation density N_S of excitons in SWNTs as $1/N_S \approx L_c$ [71]. From $L_c \approx 10$ nm, we get $N_S \approx 10^2$ excitons/μm and this value is the upper limit of the exciton density in SWNTs at room temperature, which leads to the strong optical nonlinearlity of SWNTs. Our experimental determination of L_c thus provides the further insight of the exciton transport and optical properties in SWNTs.

2.3.3 Exciton-Exciton Interaction in Carbon Nanotube

In the higher photoexcitation regime, the exciton-exciton interaction and multi-exciton dynamics appear in single SWNT PL spectra and their linewidths. The single carbon nanotube PL spectroscopy will provide insights into the exciton-dephasing and exciton-exciton interactions in a SWNT. Here, we examined the excitation power dependence of PL spectra from spatially isolated single SWNTs using singe carbon-nanotube PL spectroscopy. In the high excitation regime, the homogeneous linewidth broadens nonlinearly with an increase in excitation intensity. Our observation suggests that the broadening of homogeneous linewidth arises from the annihilation of excitons through a rapid Auger recombination process.

Figure 2.25(a) shows the temperature dependence of the PL spectra of an isolated SWNT excited with a He-Ne laser. The spectra were measured under lower excitation conditions (less than ≈ 100 μW) from 4.7 to 90 K. The PL spectra clearly narrow when the temperature decreases [74]. As indicated by the circles in the figure, the spectral lineshapes are well fitted by Lorentzian functions. The linewidth (full-width at half-maximum, FWHM) of a single SWNT, corresponding to a homogeneous linewidth is plotted as a function of temperature in Fig. 2.25(b). The temperature dependence of the linewidth shows almost linear behavior (as indicated by a solid line) in the range of 5 to 90 K. The inset of Fig. 2.25(b) shows the temperature dependence of the PL peak energy. The energy change from 5 to 90 K (≈ 1 meV) is much smaller than that in other compound semiconductor quantum
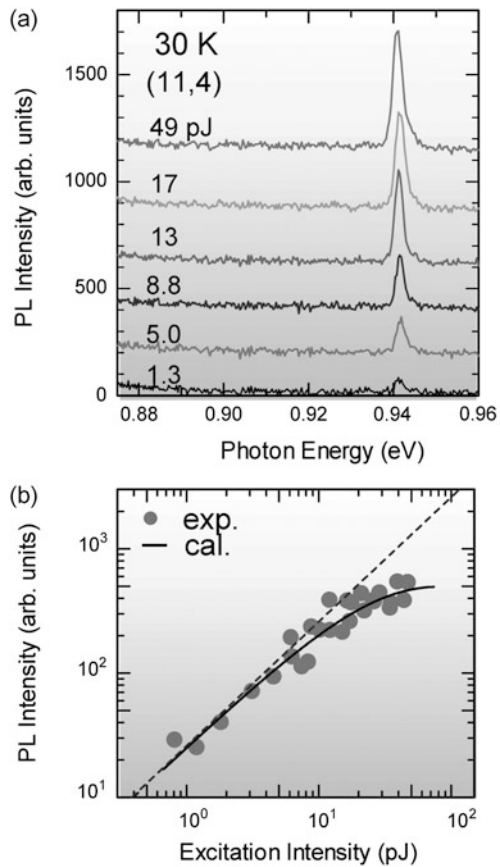
Fig. 2.25 (**a**) Temperature dependence of PL spectra of a single SWNT from 4.7 to 90 K excited with He-Ne laser light. *Solid circles* denote the Lorentzian function fits. (**b**) Spectral linewidths (full-width at half-maximum, FWHM) as a function of temperature. The *dotted line* represents the spectral resolution. The *solid line* indicates almost linear temperature dependence. *Inset* shows the temperature dependence of the PL peak energy (Reprinted with permission from [53]. Copyright, American Physical Society)
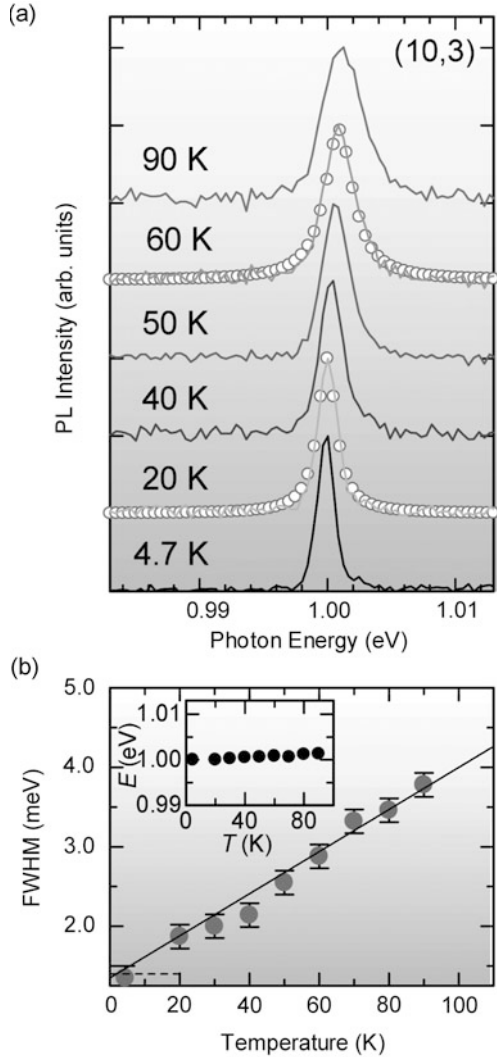
wire (12 meV from 5 to 90 K in GaAs wires) in the weak exciton-phonon coupling regime [75]. This weak temperature dependence is consistent with the experimental fact of narrow PL spectra with Lorentzian lineshape in Fig. 2.25(a).

Both the dephasing time and the lifetime of the excitons contribute to homogeneous linewidth broadening. The measured PL lifetimes of excitons are considerably longer ($\geq$20 ps) from 10 to 300 K [64], and this contribution to the linewidth is negligibly small ($\leq$0.01 meV) under lower excitation conditions. Thus, the temperature-dependent linewidths are determined approximately by the dephasing time of the exciton due to the exciton-phonon interactions. This linear temperature dependence implies that the very low energy phonon modes ($\ll k_B T$) dominate the exciton-
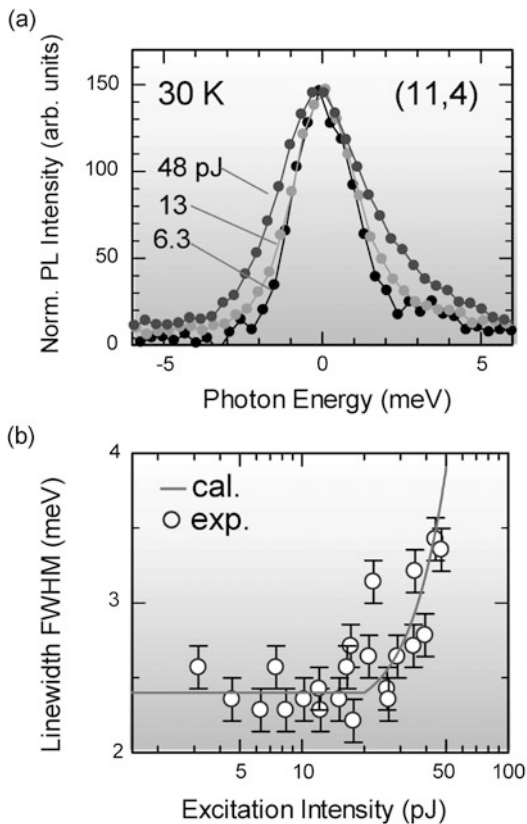
dephasing. The contributed low energy phonon to the exciton-dephasing is assigned
as the TW (twisting) mode in SWNTs [26]. Based on the homogeneous linewidth,
the exciton-dephasing time is evaluated from 350 fs at 90 K to more than 940 fs at
5 K.

Figure 2.26(a) shows PL spectra obtained from a typical single SWNT [assigned
chiral index: (11,4)] at 30 K and at various excitation intensities of 1.72-eV and
150-fs laser pulses. Each spectrum has a single peak located at 0.941 eV. Even in
the high-excitation region above about 15 pJ per pulse, the PL spectrum shows a
single peak, without a change in the peak energy. Furthermore, additional spectral
structures are not observed in any lower energy regions. Similarly, the PL bands due
to biexcitons (M-line) and inelastic exciton scattering (P-line) are not observed in
this spectral region.

Spectrally integrated PL intensities are plotted as a function of excitation laser in-
tensity in Fig. 2.26(b). In a low excitation region below 10 pJ, the PL intensity grows
almost linearly with excitation intensity (as indicated by a dotted line). Conversely,

in the higher excitation intensity region (>20 pJ), saturation of the PL intensity is clearly apparent.

We show normalized PL spectra for a single SWNT, excited with different intensities, on an expanded energy scale in Fig. 2.27(a). The spectral linewidth broadens with increasing excitation intensity. The homogeneous linewidth is plotted in Fig. 2.27(b) as a function of excitation intensity, with the FWHM of the linewidth broadening nonlinearly. This broadening cannot be explained by laser heating effects because the nonlinear broadening behavior contradicts the linear temperature dependence of the linewidth broadening [see Fig. 2.25(b)]. This excitation intensity-dependent linewidth broadening indicates that the exciton dynamics are strongly affected by the multiple excitons present in a SWNT.

Under higher excitation conditions, when additional homogeneous linewidth broadening and saturation of the PL intensity occur, more than one exciton is created in a SWNT, leading to a remarkable scattering process between excitons. Exciton-exciton annihilation occurs due to the rapid Auger nonradiative recombination process through strong Coulomb interactions [66, 76, 77]. The exciton annihilation rate $(1/\tau_{ex\text{-}ex})$ is given by [66]

$$1/\tau_{ex\text{-}ex} = ALN(N-1), \tag{2.14}$$

where A is the exciton annihilation (Auger) constant, L (≈ 1 μm) the length of the SWNT, and N the time-averaged exciton number. The exciton number should be a discrete value. However, the exciton number fluctuates at each single excitation event. Then, we might consider that the time-averaged exciton number N changes continuously in the analysis of the time-averaged PL data. Taking the radiative lifetime ($\tau_{rad} > 1$ ns) and the nonradiative lifetime, due to the exciton trapping of the nonradiative centers ($\tau_{non\text{-}rad} \approx 40$ ps) [64] into consideration, the PL intensity I_{PL} at the excitation power P is described by,

$$I_{PL} \propto \tau_{rad}^{-1} P / \left(\tau_{rad}^{-1} + \tau_{non\text{-}rad}^{-1} + \tau_{ex\text{-}ex}^{-1} \right). \tag{2.15}$$

The PL intensity saturation at higher excitation regions, as shown in Fig. 2.26(b), can be explained by the opening of the nonradiative relaxation path due to the exciton-exciton annihilation. The homogeneous linewidth Γ in Fig. 2.27(b) is determined by both the excitation power independent exciton-phonon interaction term $\Gamma_{ex\text{-}ph}$ and the excitation power dependent Auger term $\Gamma_{ex\text{-}ex}(\propto 1/\tau_{ex\text{-}ex})$,

$$\Gamma = \Gamma_{ex\text{-}ph} + \Gamma_{ex\text{-}ex}. \tag{2.16}$$

The homogeneous linewidth broadening at higher excitation regions, as shown in Fig. 2.27(a), can be explained by the shortening of exciton lifetime due to the Auger process. The nonlinear behaviors of the PL intensity and the homogeneous linewidth broadening can be reproduced using Eqs. (2.14)–(2.16) as indicated by the solid lines in Figs. 2.26(b) and 2.27(b). The time-averaged exciton number N can be translated from the excitation intensity P at which the PL intensity saturates. The best fitted curves in Figs. 2.26(b) and 2.27(b) with varying the fitting parameter A reproduced the experimental results well. Then, the derived exciton-exciton annihilation constant A of 1.6 ps^{-1} μm is almost consistent with the theoretically calculated value based on perturbation theory [66]. From this result, it was found that the multiparticle Auger process occurs very efficiently with an Auger recombination time estimated at 800 fs for ≈ 1 μm-long SWNT when two excitons are present in a SWNT. This very short time constant in comparison to bulk semiconductors, is characteristics of low-dimensional systems, including SWNTs and is comparable to the exciton-dephasing time at low temperature. These results indicate that the exciton dephasing is limited under high excitation conditions, not by the exciton-phonon interactions, but by the exciton-exciton interactions. As discussed above, the nonradiative Auger recombination process occurs efficiently at about 1 ps order. As a result, one of the two excitons nonradiatively relaxes in the ground state when two excitons are present in a SWNT. The exciton-exciton scattering rate in a SWNT is much higher than in other 1D semiconductors.

2.3.4 Multi-Exciton Generation in Carbon Nanotube

The strong enhancement of Coulomb interaction also would cause the many-body effects of excitons such as exciton multiplication (or carrier multiplication) process

Fig. 2.28 Transient absorption ($\Delta T/T$) dynamics under 1.55 eV excitation at different intensities of 15, 30, 100, and 300 μJ/cm^2. Transient absorption decays with various excitation intensities normalized by the long decay component $t = 10$ ps (Reprinted with permission from [87]. Copyright, American Institute of Physics)
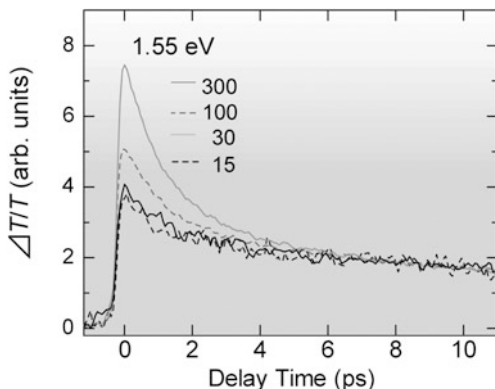
in SWNTs, where the exciton multiplication (or carrier multiplication) is the production process of two or more excitons (electron-hole pairs) by one high-energy photon well above the lowest exciton transition energy. In addition to the strong Coulomb interactions between excitons (carriers), the relaxation of momentum conservation in nanoscale space allows the observation of highly efficient exciton multiplication phenomena in a variety of nano-structures [78–82]. The achievement of efficient exciton multiplication in semiconductors makes it possible to produce highly efficient solar cells with conversion efficiencies that exceed the Shockley-Queisser limit of 32 % [83, 84]. Here, we describe exciton multiplication phenomena in CoMoCAT-SWNTs observed using femtosecond pump-probe spectroscopy.

Figure 2.28 shows the transient absorption decay monitored at E_{11} exciton absorption (1.2 eV) excited by 1.55 eV. It is clear that the temporal profile cannot be described by a single exponential function and that three exponential components (time constants of $\approx$1 ps, $\approx$30 ps, and $\approx$1 ns) appear. The decay times of $\approx$30 ps is consistent with those obtained using transient PL spectroscopy. These decays are determined by the trapping of excitons at defects of excitons in SWNTs. Hereafter, we focus on the transient absorption changes of the fast decay components on a picosecond time scale to clarify the exciton multiplication mechanism and fast Auger (exciton-exciton annihilation) nonradiative recombination.

Figure 2.28(a) shows the excitation intensity dependence of the transient absorption decay from 15 to 300 μJ/cm^2 under 1.55 eV excitation. The observed signals correspond to absorption bleaching due to excitons in SWNTs. The decay profiles at longer delay times ($t > 10$ ps) does not depend on the excitation intensity. Then, all the data are normalized at 10 ps delay time, and the normalized signal curves provide clear information about the excitation intensity-dependence of the exciton population dynamics. The fast-decay component ($t < 5$ ps) grows at increasing excitation power densities, and this excitation dependent signal above 50 μJ/cm^2 comes from the Auger (exciton-exciton annihilation) process on several picoseconds time-scale [85, 86].

Figure 2.29 shows the transient absorption dynamics under a weak excitation density at photon energies of 1.55, 3.10, and 4.65 eV, where all of the decay curves
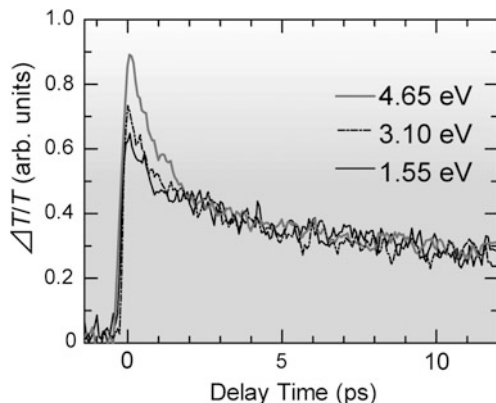
Fig. 2.29 Normalized transient absorption decays under the weak excitation regime with different excitation photon energies *black solid line*: 4.65 eV, *blue broken line*: 3.10 eV, and *red line*: 1.55 eV. This figure explains how to determine the exciton multiplication efficiency, η, which is calculated from the ratio of the transient absorption signals at zero delay (Reprinted with permission from [87]. Copyright, American Institute of Physics)

are normalized for a long time delay ($t = 10$ ps) [87]. We experimentally confirmed that in these weak intensity regions, the transient decay dynamics is independent of the excitation density. The fast-decay component due to Auger recombination does not appear in the decay curve under 1.55 and 3.10 eV excitation. Note that the decay dynamics under 4.65 eV excitation is faster than that under 1.55 eV excitation, and that the lifetime of the fast-decay component under 4.65 eV excitation is the same as the Auger recombination lifetime under intense 1.55 eV excitation. This experimental result indicates that Auger recombination occurs under 4.65 eV excitation, even in the weak-intensity region. Since the transient absorption signals of the Auger recombination process are a sign that more than two excitons are generated in a SWNT, we conclude that a single photon with an energy of 4.65 eV produces two or more excitons under weak excitation conditions, that is, exciton multiplication occurs in a SWNT [88, 89].

We can evaluate the exciton multiplication quantum efficiency (η), defined as the average number of excitons produced by one photon excitation, according to the procedures by Schaller *et al.* [89]. The $\Delta T/T$ signal amplitude is proportional to the number of excited excitons in the sample. In the ensemble experiment, the exciton density can be determined from signal amplitudes at zero delay in the time profiles normalized at a long delay time [89]. The intensity ratio of a/b at zero delay corresponds to η, where a and b are the amplitudes under 4.65 eV and 1.55 eV excitation at zero delay, respectively. In our experiment, η is estimated to be about 1.3 (130 %) under 4.65 eV excitation, while η is almost 1 within the experimental error at 3.10 eV excitation. This indicates that the novel photoelectric conversion process of exciton multipilation efficiently occurs in the SWNTs.

2.4 Summary

In this chapter, we described novel excitonic properties of carbon nanotubes revealed by single-nanotube spectroscopy and time-resolved spectroscopy. Due to the enhanced Coulomb interaction, the optically generated electron-hole pair forms a strongly bound "exciton" state, analogous to the hydrogen-like state in the carbon nanotubes. The striking properties of excitons in the carbon nanotube, such as multiple-exciton states, charged exciton (trion) formation, and exciton-multiplication were described in this chapter.

Multiple-exciton states, which affect the optical properties of carbon nanotubes, were attributed to spin degeneracy and the degenerate electronic structure of the K and K' valleys in momentum space. The singlet-bright exciton and -dark exciton, with a splitting on the order of a few meV, were revealed using the Aharonov-Bohm effect via low-temperature magneto-PL spectroscopy of a single SWNT. We identified the K-momentum dark exciton states lying approximately 40 meV above the singlet-bright exciton state from the temperature and tube-diameter dependences of the PL spectra of a single SWNT. The PL spectra showed large singlet-triplet exciton splitting, on the order of 70 meV, following pulsed-laser irradiation. We described the first observation of trions (charged excitons), three-particle bound states consisting of one electron and two holes, in hole-doped carbon nanotubes at room temperature. The unexpectedly large energy separation between the bright excitons and the trions is attributed to the strong electron-hole exchange interaction in carbon nanotubes.

The novel exciton dynamics in carbon nanotubes were revealed. We described that the very slow exciton relaxation from the bright to the dark state, and excitons are nonequilibriumly distributed between the bright and dark states due to the different parities of the wave functions. The radiative lifetimes and the 1D exciton coherence lengths in carbon nanotubes were evaluated. We found that the exciton coherence lengths in SWNTs are of the order of 10 nm, as deduced from the experimentally obtained radiative lifetimes, and they are about ten times larger than the exciton Bohr radius along the tube axis. We also observed novel exciton many body effects such as exciton (carrier) multiplication in carbon nanotubes at room temperature. These novel excitonic properties of carbon nanotube will also facilitate the future optical application based on carbon nanotubes.

References

1. S. Iijima, T. Ichihashi, Nature (London) **363**, 603 (1993)
2. R. Saito, G. Dresselhaus, M.S. Dresselhaus, *Physical Properties of Carbon Nanotubes* (Imperial College Press, London, 1998)
3. M.S. Dresselhaus, G. Dresselhaus, P. Avouris, *Carbon Nanotubes* (Springer, Berlin, 2001)
4. A. Jorio, G. Dresselhaus, M.S. Dresselhaus, *Carbon Nanotubes: Advanced Topics in the Synthesis, Structure, Properties, and Applications* (Springer, Berlin, 2008)
5. R. Saito, M. Fujita, G. Dresselhaus, M.S. Dresselhaus, Appl. Phys. Lett. **60**, 2204 (1992)

6. H. Kataura, Y. Kumazawa, Y. Maniwa, I. Umezu, S. Suzuki, Y. Ohtsuka, Y. Achiba, Synth. Met. **103**, 2555 (1999)
7. M.J. O'Connell, S.M. Bachilo, X.B. Huffman, V.C. Moore, M.S. Strano, E.H. Haroz, K.L. Rialon, P.J. Boul, W.H. Noon, C. Kittrell, J. Ma, R.H. Hauge, R.B. Weisman, R.E. Smalley, Science **297**, 593 (2002)
8. S.M. Bachilo, M.S. Strano, C. Kittrell, R.H. Hauge, R.E. Smalley, R.B. Weisman, Science **298**, 2361 (2002)
9. J. Lefebvre, Y. Homma, P. Finnie, Phys. Rev. Lett. **90**, 217401 (2003)
10. R.B. Weisman, S.M. Bachilo, Nano Lett. **3**, 1235 (2003)
11. T. Ando, J. Phys. Soc. Jpn. **66**, 1066 (1997)
12. C.L. Kane, E.J. Mele, Phys. Rev. Lett. **90**, 207401 (2003)
13. T.G. Pedersen, Phys. Rev. B **67**, 073401 (2003)
14. V. Perebeinos, J. Tersoff, Ph. Avouris, Phys. Rev. Lett. **92**, 257402 (2004)
15. H. Zhao, S. Mazumdar, Phys. Rev. Lett. **93**, 157402 (2004)
16. E. Chang, G. Bussi, A. Ruini, E. Molinari, Phys. Rev. Lett. **92**, 196401 (2004)
17. C.D. Spataru, S. Ismail-Beigi, R.B. Capaz, S.G. Louie, Phys. Rev. Lett. **95**, 247402 (2005)
18. F. Wang, G. Dukovic, L.E. Brus, T.F. Heinz, Science **308**, 838 (2005)
19. J. Maultzsch, R. Pomraenke, S. Reich, E. Chang, D. Prezzi, A. Ruini, E. Molinari, M.S. Strano, C. Thomsen, C. Lienau, Phys. Rev. B **72**, 241402(R) (2005)
20. G. Dukovic, F. Wang, D. Song, M.Y. Sfeir, T.F. Heinz, L.E. Brus, Nano Lett. **5**, 2314 (2005)
21. T. Ando, J. Phys. Soc. Jpn. **75**, 024707 (2006)
22. A. Hartschuh, H.N. Pedrosa, L. Novotny, T.D. Krauss, Science **301**, 1354 (2003)
23. J. Lefebvre, J.M. Fraser, P. Finnie, Y. Homma, Phys. Rev. B **69**, 075403 (2004)
24. K. Matsuda, Y. Kanemitsu, K. Irie, T. Saiki, T. Someya, Y. Miyauchi, S. Maruyama, Appl. Phys. Lett. **86**, 123116 (2005)
25. D.E. Milkie, C. Staii, S. Paulson, S. Paulson, E. Hindman, A.T. Johnson, J.M. Kikkawa, Nano Lett. **5**, 1135 (2005)
26. T. Inoue, K. Matsuda, Y. Murakami, S. Maruyama, Y. Kanemitsu, Phys. Rev. B **73**, 233401 (2006)
27. S. Maruyama, R. Kojima, Y. Miyauchi, S. Chiashi, M. Kohno, Chem. Phys. Lett. **360**, 229 (2002)
28. S. Zaric, G.N. Ostojic, J. Kono, J. Shaver, V.C. Moore, M.S. Strano, R.H. Hauge, R.E. Smalley, X. Wei, Science **304**, 1129 (2004)
29. S. Zaric, G.N. Ostojic, J. Shaver, J. Kono, O. Portugall, P.H. Frings, G.L.J.A. Rikken, M. Furis, S.A. Crooker, X. Wei, V.C. Moore, R.H. Hauge, R.E. Smalley, Phys. Rev. Lett. **96**, 016406 (2006)
30. J. Shaver, J. Kono, O. Portugall, V. Krstic, G.L.J.A. Rikken, Y. Miyauchi, S. Maruyama, V. Perebeinos, Nano Lett. **7**, 1851 (2007)
31. I.B. Mortimer, R.J. Nicholas, Phys. Rev. Lett. **98**, 027404 (2007)
32. R. Matsunaga, K. Matsuda, Y. Kanemitsu, Phys. Rev. Lett. **101**, 147404 (2008)
33. A. Srivastava, H. Htoon, V.I. Klimov, J. Kono, Phys. Rev. Lett. **101**, 087402 (2008)
34. K. Matsuda, T. Inoue, Y. Murakami, S. Maruyama, Y. Kanemitsu, Phys. Rev. B **77**, 033406 (2008)
35. K. Matsuda, T. Inoue, Y. Murakami, S. Maruyama, Y. Kanemitsu, Phys. Rev. B **77**, 193405 (2008)
36. K. Yoshikawa, R. Matsunaga, K. Matsuda, Y. Kanemitsu, Appl. Phys. Lett. **94**, 093109 (2009)
37. H. Ajiki, T. Ando, J. Phys. Soc. Jpn. **62**, 1255 (1993)
38. O. Kiowski, K. Arnold, S. Lebedkin, F. Hennrich, M.M. Kappes, Phys. Rev. Lett. **99**, 237402 (2007)
39. O.N. Torrens, M. Zheng, J.M. Kikkawa, Phys. Rev. Lett. **101**, 157401 (2008)
40. Y. Murakami, B. Lu, S. Kazaoui, N. Minami, T. Okubo, S. Maruyama, Phys. Rev. B **79**, 195407 (2009)
41. H. Harutyunyan, T. Gokus, A.A. Green, M.C. Hersam, M. Allegrini, A. Hartschuh, Nano Lett. **9**, 2010 (2009)

42. K. Iakoubovskii, N. Minami, Y. Kim, K. Miyashita, S. Kazaoui, B. Nalini, Appl. Phys. Lett. **89**, 173108 (2006)
43. R. Matsunaga, K. Matsuda, Y. Kanemitsu, Phys. Rev. B **81**, 033401 (2010)
44. Y. Miyauchi, S. Maruyama, Phys. Rev. B **74**, 035415 (2006)
45. R.B. Capaz, C.D. Spataru, S. Ismail-Beigi, S.G. Louie, Phys. Status Solidi (b) **244**, 4016 (2007)
46. R.B. Capaz, C.D. Spataru, S. Ismail-Beigi, S.G. Louie, Phys. Rev. B **74**, 121401(R) (2006)
47. Y. Ohno, S. Iwasaki, Y. Murakami, S. Kishimoto, S. Maruyama, T. Mizutani, Phys. Rev. B **73**, 235427 (2006)
48. A.H. Castro Neto, F. Guinea, Phys. Rev. Lett. **103**, 026804 (2009)
49. K. Nagatsu, S. Chiashi, S. Konabe, Y. Homma, Phys. Rev. Lett. **105**, 157403 (2010)
50. S. Konabe, K. Watanabe, Phys. Rev. B **83**, 045407 (2011)
51. R. Matsunaga, K. Matsuda, Y. Kanemitsu, Phys. Rev. Lett. **106**, 037404 (2011)
52. Y. Miyauchi, H. Hirori, K. Matsuda, Y. Kanemitsu, Phys. Rev. B **80**, 081410(R) (2009)
53. K. Matsuda, Y. Miyauchi, T. Sakashita, Y. Kanemitsu, Phys. Rev. B **81**, 033409 (2010)
54. T.F. Rønnow, T.G. Pedersen, H.D. Cornean, Phys. Lett. A **373**, 1478 (2009)
55. T.F. Rønnow, T.G. Pedersen, H.D. Cornean, Phys. Rev. B **81**, 205446 (2010)
56. K. Watanabe, K. Asano, Phys. Rev. B **85**, 035416 (2012)
57. S.M. Santos, B. Yuma, S. Berciaud, J. Shaver, M. Gallart, P. Gilliot, L. Congnet, B. Lounis, Phys. Rev. Lett. **107**, 187401 (2011)
58. R. Matsunaga, Y. Miyauchi, K. Matsuda, Y. Kanemitsu, Phys. Rev. B **80**, 115436 (2009)
59. M. Nirmal, D.J. Norris, M. Kuno, M.G. Bawendi, Al.L. Efros, M. Rosen, Phys. Rev. Lett. **75**, 3728 (1995)
60. A. Hagen, M. Steiner, M.B. Raschke, C. Lienau, T. Hertel, H. Qian, A.J. Meixner, A. Hartschuh, Phys. Rev. Lett. **95**, 197401 (2005)
61. V. Perebeinos, J. Tersoff, Ph. Avouris, Nano Lett. **5**, 2495 (2005)
62. J. Feldmann, G. Peter, E.O. Göbel, P. Dawson, K. Moore, C. Foxon, R.J. Elliott, Phys. Rev. Lett. **59**, 2337 (1987)
63. S. Lebedkin, F. Hennrich, O. Kiowski, M.M. Kappes, Phys. Rev. B **77**, 165429 (2008)
64. H. Hirori, K. Matsuda, Y. Miyauchi, S. Maruyama, Y. Kanemitsu, Phys. Rev. Lett. **97**, 257401 (2006)
65. Y. Miyauchi, K. Matsuda, Y. Kanemitsu, Phys. Rev. B **80**, 235433 (2009)
66. F. Wang, Y. Wu, M.S. Hybertsen, T.F. Heinz, Phys. Rev. B **73**, 245424 (2006)
67. S. Berciaud, L. Cognet, B. Lounis, Phys. Rev. Lett. **101**, 077402 (2008)
68. R.M. Russo, E.J. Mele, C.L. Kane, I.V. Rubtsov, M.J. Therien, D.E. Luzzi, Phys. Rev. B **74**, 041405(R) (2006)
69. S. Berger, C. Voisin, G. Cassabois, C. Delalande, P. Roussigno, Nano Lett. **7**, 398 (2007)
70. A. Grüneis, R. Saito, Ge.G. Samsonidze, T. Kimura, M.A. Pimenta, A. Jorio, A.G. Souza Filho, G. Dresselhaus, M.S. Dresselhaus, Phys. Rev. B **67**, 165402 (2003)
71. T. Takagahara, Solid State Commun. **78**, 279 (1991)
72. L. Cognet, D.A. Tsyboulski, J.-D.R. Rocha, C.D. Doyle, J.M. Tour, R.B. Weisman, Science **316**, 1465 (2007)
73. K. Yoshikawa, K. Matsuda, Y. Kanemitsu, J. Phys. Chem. C **114**, 4353 (2010)
74. J. Lefebvre, P. Finnie, Y. Homma, Phys. Rev. B **70**, 045419 (2004)
75. A.V. Gopal, R. Kumar, A.S. Vengurlekar, T. Mélin, F. Laruelle, B. Etienne, Appl. Phys. Lett. **74**, 2474 (1999)
76. Y.-Z. Ma, L. Valkunas, S.L. Dexheimer, S.M. Bachilo, G.R. Fleming, Phys. Rev. Lett. **94**, 157402 (2005)
77. L. Huang, T.D. Krauss, Phys. Rev. Lett. **96**, 057407 (2006)
78. R.D. Schaller, V.I. Klimov, Phys. Rev. Lett. **92**, 186601 (2004)
79. R. Ellingson, M.C. Beard, J.C. Johnson, P. Yu, O.I. Micic, A.J. Nozik, A. Shabaev, A.L. Efros, Nano Lett. **5**, 865 (2005)
80. R.D. Schaller, M.A. Petruska, V.I. Klimov, Appl. Phys. Lett. **87**, 253102 (2005)

81. M.C. Beard, K.P. Knutsen, P. Yu, J.M. Luther, Q. Song, W.K. Metzger, R.J. Ellingson, A.J. Nozik, Nano Lett. **7**, 2506 (2007)
82. J.J.H. Pijpers, E. Hendry, M.T.W. Milder, R. Fanciulli, J.L. Herek, D. Vanmaekelbergh, S. Ruhman, D. Mocatta, D. Oron, A. Aharoni, U. Banin, M. Bonn, J. Phys. Chem. C **111**, 4146 (2007)
83. W. Shockley, H.J. Queisser, J. Appl. Phys. **32**, 510 (1961)
84. V.I. Klimov, Appl. Phys. Lett. **89**, 123118 (2006)
85. F. Wang, G. Dukovic, E. Knoesel, L.E. Brus, T.F. Heinz, Phys. Rev. B **70**, 241403(R) (2004)
86. L. Valkunas, Y.-Z. Ma, G.R. Fleming, Phys. Rev. B **73**, 115432 (2006)
87. A. Ueda, K. Matsuda, T. Tayagaki, Y. Kanemitsu, Appl. Phys. Lett. **92**, 233105 (2008)
88. S. Wang, M. Khafizov, X.M. Tu, M. Zheng, T.D. Krauss, Nano Lett. **10**, 2381 (2010)
89. R.D. Schaller, M. Sykora, S. Jeong, V.I. Klimov, J. Phys. Chem. B **110**, 25332 (2006)